

Narrowband Observations of Comet 46P/Wirtanen During its Exceptional Apparition of 2018/19 II: Photometry, Jet Morphology, and Modeling Results

MATTHEW M. KNIGHT,^{1,2} DAVID G. SCHLEICHER,³ AND TONY L. FARNHAM²

¹*United States Naval Academy, Department of Physics, 572C Holloway Rd, Annapolis, MD 21402, USA*

²*University of Maryland, Department of Astronomy, College Park, MD 20742, USA*

³*Lowell Observatory, 1400 W. Mars Hill Rd, Flagstaff, AZ 86001, USA*

(Received December 24, 2020; Accepted March 16, 2021)

Submitted to the A'Hearn Symposium special issue of *The Planetary Science Journal*

ABSTRACT

We report on our extensive photometry and imaging of Comet 46P/Wirtanen during its 2018/19 apparition and use these data to constrain modeling of Wirtanen's activity. Narrowband photometry was obtained on nine epochs from 2018 October through 2019 March as well as 10 epochs during the 1991, 1997, and 2008 apparitions. The ensemble photometry reveals a typical composition and a secular decrease in activity since 1991. Production rates were roughly symmetric around perihelion for the carbon-bearing species (CN, C₃, and C₂), but steeper for OH and NH outbound. Our imaging program emphasized CN, whose coma morphology and lightcurve yielded rotation periods reported in a companion paper (Farnham et al., PSJ, 2, 7). Here, we compare the gas and dust morphology on the 18 nights for which observations of additional species were obtained. The carbon-bearing species exhibited similar morphology that varied with rotation. OH and NH had broad, hemispheric brightness enhancements in the tailward direction that did not change significantly with rotation, which we attribute to their originating from a substantial icy grain component. We constructed a Monte Carlo model that replicates the shape, motion, and brightness distribution of the CN coma throughout the apparition with a single, self-consistent solution in principal axis rotation. Our model yields a pole having (R.A., Decl.) = 319°, -5° (pole obliquity of 70°) and two large sources (radii of 50° and 40°) centered at near-equatorial latitudes and separated in longitude by ~160°. Applications of the model to explain observed behaviors are discussed.

Keywords: Comets (280); Short period comets (1452); Comet nuclei (2160); Comet volatiles (2162); Comae (271); Near-Earth objects (1092)

1. INTRODUCTION

Comet 46P/Wirtanen was discovered in 1948 by Carl Wirtanen at Lick Observatory (Jeffers 1948). Despite being observed at every perihelion since then except 1980 (e.g., Kronk 2009; Kronk & Meyer 2010; Kronk et al. 2017), little was known about it prior to its selection as the target of the *Rosetta* mission in 1994. Despite a relatively unfavorable apparition in 1997, many investigations were undertaken in order to characterize Wirtanen before *Rosetta* launched, notably includ-

ing the measurement of its small nucleus size (radius ~0.6 km; Lamy et al. 1998) and thus very high active fraction (Farnham & Schleicher 1998). Ultimately, delays in *Rosetta*'s launch caused Wirtanen to be scrapped in favor of comet 67P/Churyumov-Gerasimenko in 2004 (Ulamec et al. 2006). Wirtanen's favorable orbit has continued to make it a compelling mission target, leading to its selection for at least one subsequent mission proposal – Comet Hopper, a finalist for a NASA Discovery mission in 2011.

In the last century, Wirtanen's orbit has undergone a series of perturbations from Jupiter that have resulted in both smaller perihelion distances and shorter orbital periods. The most recent significant pertur-

bation, in 1984, reduced its perihelion distance to 1.08 AU. As a result, the 2018/19 apparition was its most favorable on record, and the close approach distance of 0.0775 AU is the 14th closest approach of a comet to Earth in the last 200 years¹. Wirtanen was more active than other recent close approaching comets including 209P/LINEAR, 45P/Honda-Mrkos-Pajdušáková, and 41P/Tuttle-Giacobini-Kresák. As a result, Wirtanen’s 2018/19 apparition was one of the best observing opportunities for a Jupiter family comet in many years, particularly for northern hemisphere observers, and it was the target of a widespread observation campaign. Results published so far include measurements of the nucleus’ rotation period (Farnham et al. 2021), detections of at least five small (<1.5 mag) outbursts and discovery of a dust trail (Farnham et al. 2019, 2021; Kelley et al. 2019, 2020), the first measurement of the D/H ratio (Lis et al. 2019), and detection of HCN (Wang et al. 2020).

We planned an extensive campaign using the telescopes at Lowell Observatory to conduct photoelectric photometry and imaging at near-UV and optical wavelengths. Our objectives during the 2018/19 apparition were numerous and designed to capitalize on the rare opportunity to observe the comet while it was bright for several months over a wide range of viewing geometries and at high spatial resolution. These included obtaining extensive photoelectric photometry for comparison to previous datasets to look for secular evolution and better quantify seasonal behaviors, identifying diagnostic features in the gas and dust coma, and using the motion and repetition of these features to constrain the nucleus’ rotation period at one or more epochs. Ultimately, we collected usable data on more than 40 nights and were able to construct a detailed model of the nucleus including the location and extent of source regions and orientation of the rotation pole.

Results of our extensive CN imaging, including identification of at least two gas jets and evidence for the nucleus being in simple rotation with an apparent period that increased from 8.98 hr to 9.14 hr, then decreased to 8.94 hr, are discussed in a companion paper, Farnham et al. (2021) and henceforth referred to as Paper I. The current paper presents complementary analyses, some of which rely on the results from Paper I. Observations and reductions are summarized in Section 2. In Section 3 we analyze photometry from this and three previous apparitions. In Section 4 we discuss the coma morphology of dust and gas species other than CN. The

photometry and imaging are used as constraints for our Monte Carlo model in Section 5. The results and conclusions are discussed in Sections 6 and 7, respectively.

2. OBSERVATIONS AND REDUCTIONS

2.1. CCD Observations and Reductions

As discussed in Paper I, we imaged Wirtanen extensively throughout the 2018/19 apparition using the telescopes at Lowell Observatory. We made the first successful recovery of the apparition in June 2018 (Feaga et al. 2018) and monitored it thereafter, but it was too faint for the studies reported here until October. Regular monitoring was conducted from late October 2018 through early February 2019 using the 31in (0.8m) telescope in robotic mode, while dedicated observing runs were made using the John S. Hall 42in (1.1m) and the 4.3-m Lowell Discovery Telescope (LDT; then called Discovery Channel Telescope or DCT) in early-November, early- and mid-December, and early- and late-January. Most 31in nights consisted of “snapshot” (one epoch of observations) or “monitoring” (two or more epochs of non-continuous observations) observations using broadband r' or R filters and a narrowband CN filter from the HB comet filter set (Farnham et al. 2000). Wirtanen was imaged nearly continuously on most 42in and LDT nights, with regular observations in R or r' and CN supplemented with other HB narrowband filters designed to isolate gas (OH, NH, C₂, C₃) or dust (UC, GC, BC, RC). A complete overview of observations is given in Table 1.

LDT images used the Large Monolithic Imager (LMI) which has a 6.1 K × 6.1 K e2v CCD with a field of view of 12.3 arcmin on a side. Depending on conditions and the observational goals for a night, images were binned on chip to either 2×2 or 3×3 resulting in pixel scales of 0.24 arcsec and 0.36 arcsec, respectively. The 42in’s NASA42 camera has an e2v CCD231-84 chip with 4 K × 4 K pixels and a field of view 25.3 arcmin on a side. On chip binning of 2×2 or 3×3 resulted in pixel scales of 0.74 arcsec and 1.11 arcsec, respectively. The 31in has a 2 K × 2 K e2v CCD42-40 with 0.46 arcsec pixels and a field of view about 15.7 arcmin on a side.

All images were acquired at the comet’s ephemeris rate. Exposure times varied with the comet’s brightness, telescope size, and time available, but were typically 30–60 sec for broadband images and 180–300 sec for narrowband images. Most filters were acquired in sets of 3–5 images which were later median combined to improve signal-to-noise and minimize the effects of background stars, bad pixels, cosmic rays, etc. When conditions were photometric during our dedicated observing runs, HB standard stars (Farnham et al. 2000)

¹ http://wirtanen.astro.umd.edu/close_approaches.shtml

Table 1. Imaging observations and geometric parameters for comet 46P/Wirtanen.^a

UT	UT	Tel. ^b	Δ T ^c	r_H ^d	Δ ^e	α ^f	P.A. ^g	Filters	Obs.	Cond. ⁱ
Date	Range		(day)	(AU)	(AU)	($^\circ$)	($^\circ$)		Type ^h	
2018 Oct 28	7:22– 7:36	31in	-45.62	1.218	0.295	35.8	183.4	R, CN	S	CLR
2018 Nov 1	4:37– 8:38	42in	-41.65	1.193	0.273	38.0	188.1	R, CN, OH, C3, C2, BC, GC	C	CIR
2018 Nov 1	5:52– 7:29	31in	-41.65	1.193	0.273	38.0	188.1	R, CN	M	CIR
2018 Nov 2	4:30– 8:55	42in	-40.65	1.187	0.267	38.6	189.2	R, CN, OH, C3, C2, BC, GC	C	CIR
2018 Nov 3	4:21– 8:53	LDT	-39.65	1.181	0.262	39.1	190.3	r' , CN	C	CLD
2018 Nov 4	4:13– 8:34	42in	-38.66	1.176	0.256	39.7	191.4	R, CN, OH, C3, C2, BC, GC	C	CIR
2018 Nov 4	5:40– 7:25	31in	-38.65	1.176	0.256	39.7	191.4	R, CN	M	CIR
2018 Nov 9	4:36– 7:48	42in	-33.67	1.148	0.229	42.3	196.6	R, CN	C	CLR
2018 Nov 10	4:36– 5:04	31in	-32.73	1.143	0.224	42.7	197.5	R, CN	S	CLR
2018 Nov 11	4:36– 5:03	31in	-31.73	1.138	0.219	43.2	198.5	R, CN	S	CLR*
2018 Nov 11	4:16– 8:01	42in	-31.67	1.138	0.219	43.2	198.6	R, CN	C	CLR*
2018 Nov 12	4:36– 5:04	31in	-30.73	1.134	0.214	43.7	199.5	R, CN	S	CLR
2018 Nov 12	4:15– 7:26	42in	-30.68	1.133	0.214	43.7	199.5	R, CN	C	CLR
2018 Nov 13	5:07– 5:27	31in	-29.71	1.129	0.208	44.1	200.4	R, CN	S	CLR
2018 Nov 13	4:34– 7:45	42in	-29.67	1.128	0.208	44.1	200.5	R, CN	C	CLR
2018 Nov 15	5:00– 5:20	31in	-27.71	1.120	0.198	44.9	202.2	R, CN	S	CLR
2018 Nov 16	4:58– 5:18	31in	-26.71	1.115	0.193	45.3	203.1	R, CN	S	CLD
2018 Nov 26	4:33– 6:16	31in	-16.70	1.079	0.143	46.7	211.3	R, CN	S	CLD
2018 Nov 27	4:29– 6:14	31in	-15.70	1.077	0.138	46.5	212.1	R, CN	S	CLR
2018 Nov 29	5:27– 6:10	31in	-13.69	1.072	0.128	45.8	213.7	R, CN	S	CLD
2018 Dec 3	2:06– 9:05	LDT	-9.69	1.064	0.111	43.3	217.3	r' , CN, OH, NH, C3, C2, UC, BC, RC	C	ICL
2018 Dec 4	1:55– 8:41	LDT	-8.71	1.062	0.107	42.3	218.3	r' , CN, OH, C3, C2, BC, RC	C	ICL
2018 Dec 5	6:05– 6:23	31in	-7.67	1.060	0.103	41.1	219.6	R, CN	S	CLR
2018 Dec 6	1:36– 6:57	LDT	-6.75	1.059	0.099	39.9	220.7	R, CN, OH	M	CLD
2018 Dec 9	1:46– 2:07	42in	-3.85	1.057	0.089	35.2	225.7	R, CN	S	CLR
2018 Dec 10	0:46–10:11	42in	-2.70	1.056	0.086	33.0	228.5	R, CN, OH, NH, C3, C2	C	CIR
2018 Dec 12	1:47– 7:10	LDT	-0.74	1.055	0.082	28.9	234.9	R, CN, OH, NH, C3, BC	C	CIR
2018 Dec 12	2:06– 9:03	31in	-0.70	1.055	0.082	28.8	235.0	R, CN	M	CIR
2018 Dec 13	1:15– 7:25	LDT	+0.25	1.055	0.080	26.7	239.2	R, CN, OH, NH, C3, BC	C	CLR
2018 Dec 14	1:08– 7:15	LDT	+1.25	1.055	0.079	24.5	244.6	R, CN, OH, NH, C3, BC	C	CLR
2018 Dec 15	1:32– 9:49	LDT	+2.31	1.056	0.078	22.3	251.7	r' , CN	C	CLD
2018 Dec 16	1:40–11:26	LDT	+3.35	1.056	0.077	20.5	260.2	r' , CN, OH, NH, C3, C2, UC, BC, RC	C	CLR
2018 Dec 17	1:30–11:18	LDT	+4.34	1.057	0.078	19.2	239.7	r' , CN, OH, NH, C3, C2, UC, BC, RC	C	CLD
2018 Dec 19	2:15–11:23	31in	+6.36	1.059	0.079	18.1	291.9	R, CN	M	CLR
2018 Dec 23	2:23– 2:41	31in	+10.18	1.064	0.087	21.1	328.5	R, CN	S	CLD
2018 Dec 24	5:24– 5:43	31in	+11.30	1.066	0.090	22.6	336.3	R, CN	S	CLD
2018 Dec 25	3:25–12:34	31in	+12.40	1.069	0.094	24.1	342.7	R, CN	M	ICL
2018 Dec 27	3:22–13:06	31in	+14.41	1.073	0.102	26.6	352.5	R, CN	M	CLD
2018 Dec 30	2:27–13:24	31in	+17.40	1.081	0.115	29.6	3.5	R, CN	M	CIR
2018 Dec 31	2:29– 4:04	31in	+18.26	1.084	0.119	30.2	6.1	R, CN	S	CLD
2019 Jan 3	1:45–13:12	42in	+21.38	1.094	0.134	32.1	13.7	R, CN, OH	C	CLR
2019 Jan 4	4:06–13:31	31in	+22.44	1.098	0.139	32.5	15.7	R, CN	S	CLR
2019 Jan 4	4:14–13:12	42in	+22.43	1.098	0.139	32.5	15.6	R, CN, OH	C	CLR
2019 Jan 5	3:42–13:30	31in	+23.43	1.102	0.145	32.8	17.3	R, CN	M	ICL
2019 Jan 12	1:43–13:40	LDT	+30.39	1.132	0.184	33.4	23.4	r' , CN, OH, BC, RC	C	ICL
2019 Jan 26	2:01–13:12	42in	+44.39	1.210	0.273	30.5	17.4	R, CN, OH	C	ICL
2019 Jan 27	2:01– 6:32	42in	+45.25	1.215	0.279	30.3	16.6	R, CN, OH	C	ICL
2019 Jan 28	2:00–13:06	42in	+46.39	1.223	0.287	30.0	15.4	R, CN, OH	C	CLR
2019 Feb 8	4:10– 4:40	31in	+57.26	1.298	0.368	27.6	1.9	R, CN	S	CLR
2019 Feb 8	4:00–13:29	42in	+57.44	1.299	0.369	27.6	1.6	R, CN	C	CLR
2019 Feb 8	2:16–12:25	LDT	+57.38	1.298	0.369	27.6	1.7	R, CN	M	CIR
2019 Feb 9	2:33– 5:34	42in	+58.24	1.305	0.376	27.4	0.6	R, CN	C	CLD

^a All parameters are given for the midpoint of each night’s observations.

^b Telescope used: LDT = Lowell Discovery Telescope (4.3-m), 42in = Hall 42-in Telescope (1.1-m), 31in = 31-in Telescope (0.8-m).

^c Time from perihelion.

^d Heliocentric distance.

^e Geocentric distance.

^f Solar phase angle.

^g Position angle of the Sun.

^h Type of observation: S = snapshot (one epoch during the night), M = monitoring (2 or more visits during a night with gaps), C = continuous (nearly continuous observations throughout the night)

ⁱ Conditions: CLR = clear, CIR = cirrus, ICL = intermittent clouds, CLD = clouds; * indicates possible smoke

were obtained to allow absolute calibrations of narrow-band images.

Images were debiased and flat-field corrected using standard procedures. Absolute calibrations of narrow-band images were performed on photometric nights following the procedures outlined in Farnham et al. (2000) to remove underlying continuum from gas images (OH, NH, CN, C₂, and C₃). The standard reduction methodology assumes a solar dust color if a particular continuum filter is not available; we found that this yielded an over-subtraction of continuum in the NH filter if the UV continuum (UC) filter was not used. Thus, we processed December 13 and 14 by assuming the UC to blue continuum (BC) ratio was the same as on December 16. We confirmed that this technique yielded comparable morphology to the standard procedure on other nights where UC and BC were both obtained, so we are confident that it could safely be used to assess morphology on these nights. We confirmed on the photometric nights that the CN and OH were minimally contaminated with dust and that the bulk morphology was unaffected by the continuum removal. Thus, we also used CN and OH for morphological studies on non-photometric nights.

We determined centroids using a 2D Gaussian fit to the inner coma and used these centroids for photometric measurements, aligning images, and for applying our standard image enhancement routines (e.g., Schleicher & Farnham 2004; Knight et al. 2017). A variety of image enhancement techniques were utilized when exploring the data, with removal of a temporal average (based on the period determined in Paper I) preferred when sufficient data were available, and removal of an azimuthal median favored otherwise. Both enhancements are relatively benign and do not introduce or significantly alter structures in the coma, although we do use caution in interpreting features within a few pixels of the center as these are most sensitive to the centroiding. When needed, Gaussian smoothing was applied to images having lower signal-to-noise ratios.

2.2. Photometer Observations and Reductions

Narrowband photometry was obtained with two traditional photoelectric photometers at the John S. Hall 42-inch (1.1-m) telescope at Lowell Observatory, except for two nights in 1997 when the 31-inch (0.8-m) telescope was used instead. The IHW filter set (Osborn et al. 1990; A’Hearn 1991; Larson et al. 1991) was utilized in 1991 and for all but one set of data in 1997, while the HB filter set was used in that one case and for all observations during the 2007/08 and 2018/19 apparitions.

Standard observing and reduction techniques and coefficients were employed for the photometric observa-

tions, as detailed by Farnham et al. (2000) for the HB filters and as revised by Farnham & Schleicher (2005) for the older IHW filters. Because these revisions for the IHW filters gave improved decontamination for the continuum filters, for completeness we re-tabulate here the adjusted values for the originally published results from Farnham & Schleicher (1998) along with the more recent apparitions. In all cases, fluxes within the entrance aperture of the photometer are converted to column abundances, $M(\rho)$, and then to production rates, Q , for each of the five observed gas species – OH, NH, CN, C₂, and C₃ (cf. A’Hearn et al. 1995). Continuum fluxes (note that wavelengths of the continuum filters changed between the two filter sets) are converted to $A(\theta)f\rho$, a proxy for dust production introduced by A’Hearn et al. (1984). Phase angle adjustments are made using the Schleicher-Marcus composite dust phase curve (see Schleicher & Bair 2011).

3. PHOTOMETRIC RESULTS

3.1. The Photometry Datasets

Since rotational studies during the 2018/19 apparition would best be conducted using imaging techniques, our goals for the photometry were primarily intended to extend our heliocentric distance coverage of Wirtanen as compared to what was obtained at prior apparitions and to search for possible secular trends. We, therefore, employed the methodology of trying to acquire one photometric night of data per observing run, with subsequent nights used for additional imaging.

This method worked quite well overall, with only two runs – in late September and late October – completely clouded out, while nine other runs were successful. Observing circumstances for these nine nights, along with four nights from 2007/08, five nights from 1997, and one from 1991, are listed in Table 2. While most nights in the first three apparitions have only a single dataset, all nights in 2018/19 have at least two sets, usually with multiple aperture sizes, and on one night we obtained 12 sets using 9 different apertures. Reduced fluxes and resulting aperture abundances are given in Table 3, while the derived gas production rates and dust $Af\rho$ values are listed in Table 4. These final results are also plotted, as logarithms, as a function of $\log r_H$ in Figure 1. Different symbols distinguish each apparition while pre- and post-perihelion data are identified by open and filled symbols, respectively. Since the photometric uncertainties ($1-\sigma$) are unbalanced in logarithmic space, only the “positive” uncertainties are tabulated, while the “negative” uncertainties can be readily calculated.

Table 2. Photometry observing circumstances and fluorescence efficiencies for comet 46P/Wirtanen.^a

UT Date	ΔT (day)	r_H (AU)	Δ (AU)	Phase ($^\circ$)	Phase Adj. ^b	\dot{r}_H (km s^{-1})	$\log L/N$ ($\text{erg s}^{-1} \text{ molecule}^{-1}$)			
							OH	NH	CN	
1991 Oct	11.5	+21.0	1.118	1.408	44.8	0.457	+5.6	-14.674	-13.157	-12.424
1997 Feb	12.1	-30.4	1.137	1.600	37.7	0.429	-8.1	-14.876	-13.226	-12.526
1997 Feb	15.1	-27.4	1.124	1.590	38.0	0.431	-7.4	-14.886	-13.215	-12.520
1997 Mar	5.1	-9.4	1.071	1.536	39.9	0.439	-2.7	-14.833	-13.251	-12.573
1997 Jun	4.2	+81.7	1.494	1.961	30.5	0.386	+14.2	-14.585	-13.469	-12.724
1997 Jul	1.2	+108.7	1.721	2.311	24.0	0.331	+14.7	-14.699	-13.595	-12.845
2007 Dec	4.2	-60.3	1.321	1.080	47.2	0.464	-12.8	-14.790	-13.379	-12.706
2008 Mar	4.2	+30.7	1.135	0.941	56.1	0.469	+8.3	-14.672	-13.158	-12.432
2008 Mar	5.2	+31.7	1.140	0.944	55.9	0.469	+8.5	-14.674	-13.164	-12.435
2008 Apr	30.2	+87.8	1.540	1.435	39.4	0.437	+14.5	-14.606	-13.498	-12.747
2018 Oct	6.3	-67.6	1.376	0.438	25.8	0.348	-13.5	-14.860	-13.415	-12.738
2018 Nov	7.3	-35.7	1.159	0.240	41.3	0.445	-9.4	-14.790	-13.253	-12.550
2018 Nov	15.3	-27.6	1.119	0.198	44.9	0.458	-7.7	-14.876	-13.212	-12.514
2018 Dec	3.2	-9.8	1.064	0.111	43.3	0.452	-2.9	-14.824	-13.240	-12.561
2018 Dec	16.3	+3.4	1.056	0.077	20.5	0.296	+1.0	-14.854	-13.220	-12.593
2018 Dec	30.1	+17.2	1.081	0.113	29.4	0.378	+5.0	-14.660	-13.138	-12.403
2019 Jan	31.2	+49.3	1.242	0.307	29.3	0.377	+11.6	-14.569	-13.278	-12.535
2019 Feb	26.2	+75.3	1.437	0.529	26.2	0.352	+14.0	-14.556	-13.434	-12.690
2019 Mar	25.2	+102.2	1.662	0.843	27.8	0.365	+14.8	-14.668	-13.567	-12.812

^a All parameters are given for the midpoint of each night’s observations.

^b Adjustment to 0° solar phase angle to $\log(A(\theta)f\rho)$ values based on adopted phase function (see text).

3.2. Gas Production Rates vs Distance, Time, and Apparition

It is immediately evident from Figure 1 that the overall quality of the data from the newest apparition is much better than that from prior years, and permits us to readily examine the slopes of the production rates with heliocentric distance. In fact the r_H -dependencies are unusually linear in log-log space. In particular, the carbon-bearing species (CN, C_3 , and C_2) exhibit very similar slopes (ranging from -3.5 to -3.7 to -3.9 , respectively) and very little difference before and after perihelion. In comparison, both OH and NH vary in a similar manner – while only slightly steeper inbound (-4.3 and -4.2 , respectively) than the carbon-bearing species, they fall-off significantly faster outbound (-5.1 and -5.2 , if one ignores the abnormally low NH point on the final night [off the plot in Fig. 1]). These results strongly imply a compositional heterogeneity between the two source regions identified in the modeling from Section 5. Several other comets have exhibited differing behavior in the carbon-bearing species and the hydrogen-bearing species, including 2P/Encke (A’Hearn et al. 1983, 1995) and 45P/Honda-Mrkos-Pajusakova (our database). However, we emphasize that the composition of both regions on the surface of Wirtanen fall

within the “typical” class of our large database (Schleicher & Bair 2016); the ratio of carbon-bearing species to water can vary by more than a factor of two and still be in the typical class.

It is also evident from examination of Figure 1 that gas production rates were significantly lower in the most recent apparition. However, before examining this decrease in more detail, we first looked for possible aperture trends that might have an effect on our derived production rates, because Wirtanen approached Earth so much closer than ever before. Looking first at the night of December 3 with its nine aperture sizes, ranging from 24 to 204 arcsec ($\rho = 980$ to 8320 km), and then other nights near closest approach, we see no trends with aperture size for OH, NH, or CN. Even C_3 and C_2 exhibit small but consistent trends (an increase of only 15% for a factor of $8\times$ in aperture radius). Larger apertures early and late in the apparition exhibit no trends at all. Therefore, we conclude that the lower gas production rates measured in 2018/19 are real.

Allowing for the observed heliocentric distance trends, when they could be reliably determined, we see an ongoing secular decrease across all four apparitions. For instance, CN decreases by $\sim 28\%$ from 1991 to 1997, $\sim 21\%$ from 1997 to 2008, and by $\sim 31\%$ from 2008 to

Table 3. Photometric fluxes and aperture abundances for comet 46P/Wirtanen.

UT Date	Aperture		log Emission Band Flux					log Continuum Flux ^a			log $M(\rho)$				
	Size	$\log \rho$	(erg cm ⁻² s ⁻¹)					(erg cm ⁻² s ⁻¹ Å ⁻¹)			(molecule)				
	(arcsec)	(km)	OH	NH	CN	C ₃	C ₂	UV	Blue	Green	OH	NH	CN	C ₃	C ₂
1991 Oct 11.5	35.3	4.26	-10.43	-11.27	-10.62	-10.87	-10.74	-14.16	...	-13.84	31.99	29.64	29.55	28.97	29.45
1997 Feb 12.1	73.7	4.63	-10.15	-11.19	-10.58	-10.83	-10.61	-14.13	...	-14.01	32.58	29.89	29.80	29.14	29.70
1997 Feb 15.1	73.7	4.63	-10.23	-11.11	-10.52	-10.68	-10.52	-13.60	...	-14.03	32.50	29.96	29.85	29.28	29.78
1997 Mar 5.1	57.6	4.51	-10.33	...	-10.55	-10.67	-10.46	-14.10	-13.77	-13.70	32.32	...	29.85	29.21	29.77
1997 Mar 5.1	57.6	4.51	-10.39	-10.95	-10.54	-10.68	-10.49	-14.07	-13.77	-13.53	32.26	30.12	29.86	29.20	29.74
1997 Mar 5.1	114.7	4.81	-9.97	-10.70	-10.19	-10.64	-10.15	-13.65	-13.77	-13.44	32.69	30.37	30.20	29.24	30.08
1997 Jun 4.2	146.7	5.02	-10.99	...	-11.00	-14.30	29.76	...	29.73
1997 Jul 1.2	114.7	4.98	-11.41	...	-11.46	-14.61	...	-14.36	29.61	...	29.53
2007 Dec 4.2	97.2	4.58	-10.38	-11.31	-10.77	-10.83	-10.68	<i>und</i>	-14.19	-14.53	31.93	29.58	29.45	28.92	29.42
2008 Mar 4.2	97.2	4.52	-9.94	-10.79	-10.17	-10.48	-10.23	-13.77	-13.53	-13.69	32.13	29.76	29.66	29.03	29.62
2008 Mar 4.2	62.4	4.33	-10.22	-11.08	-10.44	-10.65	-10.51	-14.05	-13.82	-13.76	31.85	29.48	29.39	28.86	29.34
2008 Mar 5.2	77.8	4.43	-10.11	-10.97	-10.34	-10.59	-10.40	-13.99	-13.79	-13.77	31.96	29.59	29.50	28.92	29.46
2008 Apr 30.2	77.8	4.61	-10.94	-11.93	-11.25	-11.40	-11.33	-14.72	-14.49	-14.59	31.42	29.33	29.26	28.74	29.15
2018 Oct 6.3	97.2	4.19	-10.49	-11.44	-10.85	-10.65	-10.78	-14.57	-13.70	-13.80	31.10	28.71	28.62	28.36	28.57
2018 Oct 6.3	204.5	4.51	-10.03	-10.90	-10.38	-10.31	-10.30	-14.04	-13.46	-13.50	31.56	29.25	29.09	28.69	29.05
2018 Oct 6.3	48.6	3.89	-10.96	-11.92	-11.31	-11.10	-11.27	-14.34	-13.92	-13.94	30.63	28.23	28.16	27.91	28.09
2018 Oct 6.3	97.2	4.19	-10.52	-11.46	-10.85	-10.68	-10.79	-14.20	-13.73	-13.75	31.07	28.69	28.62	28.33	28.57
2018 Nov 7.2	204.5	4.25	-9.34	-10.22	-9.66	-9.60	-9.62	-13.16	-12.73	-12.80	31.66	29.25	29.10	28.74	29.07
2018 Nov 7.3	97.2	3.93	-9.84	-10.73	-10.14	-9.97	-10.10	-13.33	-13.00	-13.03	31.16	28.74	28.62	28.37	28.58
2018 Nov 7.3	48.6	3.63	-10.35	-11.23	-10.63	-10.33	-10.61	-13.76	-13.26	-13.28	30.65	28.23	28.13	28.00	28.08
2018 Nov 7.3	97.2	3.93	-9.83	-10.72	-10.14	-9.95	-10.10	-13.45	-13.00	-13.06	31.17	28.74	28.62	28.39	28.58
2018 Nov 15.3	155.9	4.05	-9.48	-10.24	-9.70	-9.57	-9.67	-13.22	-12.64	-12.67	31.44	29.01	28.86	28.57	28.82
2018 Nov 15.3	48.6	3.54	-10.33	-11.11	-10.51	-10.22	-10.50	-13.61	-13.13	-13.15	30.59	28.15	28.05	27.92	27.99
2018 Nov 15.3	97.2	3.84	-9.83	-10.60	-10.02	-9.81	-10.00	-13.33	-12.85	-12.89	31.09	28.65	28.53	28.33	28.49
2018 Nov 15.3	155.9	4.05	-9.50	-10.26	-9.70	-9.58	-9.68	-13.20	-12.70	-12.72	31.42	29.00	28.85	28.56	28.81
2018 Nov 15.3	97.2	3.84	-9.82	-10.60	-10.03	-9.83	-10.01	-13.32	-12.86	-12.90	31.10	28.65	28.53	28.31	28.48
2018 Dec 3.1	97.2	3.59	-9.60	-10.44	-9.86	-9.52	-9.74	-12.83	-12.42	-12.46	30.76	28.34	28.24	28.07	28.20
2018 Dec 3.1	204.5	3.92	-9.10	-9.89	-9.35	-9.11	-9.21	-12.53	-12.12	-12.17	31.27	28.89	28.75	28.49	28.73
2018 Dec 3.1	48.6	3.29	-10.13	-10.97	-10.39	-9.96	-10.27	-13.13	-12.71	-12.74	30.23	27.81	27.71	27.63	27.67
2018 Dec 3.1	155.9	3.80	-9.29	-10.08	-9.53	-9.25	-9.40	-12.64	-12.23	-12.27	31.08	28.70	28.57	28.34	28.54
2018 Dec 3.1	126.7	3.71	-9.44	-10.24	-9.69	-9.37	-9.55	-12.72	-12.30	-12.35	30.93	28.54	28.41	28.22	28.39
2018 Dec 3.2	77.8	3.50	-9.78	-10.62	-10.03	-9.65	-9.91	-12.94	-12.51	-12.54	30.58	28.16	28.07	27.95	28.03
2018 Dec 3.2	62.4	3.40	-9.97	-10.81	-10.21	-9.81	-10.09	-13.02	-12.61	-12.64	30.39	27.97	27.89	27.78	27.85
2018 Dec 3.2	38.5	3.19	-10.33	-11.17	-10.55	-10.12	-10.45	-13.21	-12.81	-12.82	30.04	27.61	27.55	27.47	27.49
2018 Dec 3.2	24.5	2.99	-10.69	-11.55	-10.90	-10.45	-10.82	-13.42	-13.01	-13.03	29.68	27.23	27.20	27.15	27.12
2018 Dec 3.2	48.6	3.29	-10.16	-10.99	-10.37	-9.95	-10.28	-13.13	-12.73	-12.73	30.20	27.79	27.73	27.65	27.66
2018 Dec 3.2	97.2	3.59	-9.65	-10.44	-9.88	-9.52	-9.76	-12.85	-12.42	-12.45	30.71	28.34	28.22	28.07	28.18
2018 Dec 3.3	97.2	3.59	-9.63	-10.45	-9.87	-9.53	-9.75	-12.87	-12.43	-12.45	30.73	28.33	28.23	28.07	28.19
2018 Dec 16.3	97.2	3.43	-9.65	-10.42	-9.83	-9.41	-9.70	-12.39	-11.99	-11.99	30.42	28.02	27.99	27.86	27.92
2018 Dec 16.3	155.9	3.64	-9.31	-10.05	-9.49	-9.13	-9.35	-12.19	-11.80	-11.82	30.76	28.39	28.32	28.14	28.27
2018 Dec 16.3	48.6	3.13	-10.17	-10.95	-10.38	-9.90	-10.22	-12.70	-12.30	-12.31	29.90	27.49	27.44	27.37	27.40
2018 Dec 16.4	155.9	3.64	-9.29	-10.03	-9.49	-9.13	-9.34	-12.18	-11.79	-11.80	30.79	28.41	28.32	28.14	28.28
2018 Dec 30.1	97.2	3.60	-9.60	-10.46	-9.77	-9.63	-9.84	-12.75	-12.36	-12.40	30.61	28.23	28.19	28.00	28.13
2018 Dec 30.1	204.5	3.92	-9.08	-9.91	-9.24	-9.21	-9.30	-12.48	-12.09	-12.12	31.14	28.78	28.72	28.41	28.67
2018 Dec 30.1	48.6	3.30	-10.11	-10.99	-10.27	-10.07	-10.35	-13.07	-12.66	-12.69	30.10	27.71	27.69	27.56	27.62
2018 Dec 30.1	97.2	3.60	-9.63	-10.48	-9.77	-9.63	-9.84	-12.78	-12.39	-12.42	30.59	28.21	28.19	27.99	28.13
2019 Jan 31.2	97.2	4.03	-10.04	-11.09	-10.35	-10.35	-10.42	-13.59	-13.21	-13.25	30.95	28.62	28.61	28.26	28.53
2019 Jan 31.2	204.5	4.36	-9.54	-10.58	-9.86	-10.01	-9.91	-13.24	-12.93	-12.98	31.45	29.12	29.10	28.60	29.05
2019 Feb 26.2	97.2	4.27	-10.51	-11.80	-10.91	-10.89	-10.99	-14.44	-13.78	-13.84	30.94	28.53	28.68	28.32	28.57
2019 Feb 26.3	97.2	4.27	-10.51	-11.81	-10.91	-10.92	-11.00	-14.12	-13.85	-14.07	30.94	28.52	28.68	28.29	28.56
2019 Mar 25.2	62.4	4.28	-11.44	-13.10	-11.68	-11.69	-11.77	-14.69	-14.65	-14.51	30.53	27.77	28.43	28.05	28.32
2019 Mar 25.2	97.2	4.47	-11.07	-12.33	-11.39	-11.40	-11.48	-14.70	-14.42	-14.49	30.89	28.53	28.72	28.34	28.61

^a “*und*” stands for “undefined” and means the continuum flux was measured but was less than 0.

Table 4. Photometric production rates for comet 46P/Wirtanen.

UT Date	ΔT (day)	$\log r_H$ (AU)	$\log \rho$ (km)	$\log Q^a$ (molecules s ⁻¹)					$\log A(\theta)f\rho^b$ (cm)			$\log Q$ H ₂ O
				OH	NH	CN	C ₃	C ₂	UV	Blue	Green	
1991 Oct 11.5	+21.0	0.048	4.26	27.99 .02	25.86 .04	25.40 .01	24.78 .02	25.49 .01	1.88 .08	...	1.97 .02	28.10
1997 Feb 12.1	-30.4	0.056	4.63	28.07 .10	25.56 .15	25.18 .02	24.71 .09	25.27 .02	1.67 .36	...	1.54 .15	28.18
1997 Feb 15.1	-27.4	0.051	4.63	28.00 .04	25.62 .09	25.22 .01	24.86 .04	25.35 .01	2.18 .10	...	1.52 .06	28.10
1997 Mar 5.1	-9.4	0.030	4.51	27.96 .03	...	25.36 .01	24.87 .03	25.47 .01	1.82 .15	1.82 .07	1.91 .05	28.08
1997 Mar 5.1	-9.4	0.030	4.51	27.90 .04	25.94 .04	25.37 .01	24.86 .03	25.44 .01	1.76 .12	0.00 .07	2.07 .03	28.02
1997 Mar 5.1	-9.4	0.030	4.81	27.97 .05	25.79 .06	25.39 .01	24.79 .06	25.48 .01	1.88 .15	0.00 .07	1.86 .04	28.09
1997 Jun 4.2	+81.7	0.174	5.02	24.74 .03	...	24.91 .03	1.28 .19	...
1997 Jul 1.2	+108.7	0.236	4.98	24.64 .05	...	24.75 .08	1.51 .20	...	1.52 .20	...
2007 Dec 4.2	-60.3	0.121	4.58	27.53 .03	25.38 .10	24.92 .12	24.46 .11	25.08 .01	<i>und</i>	1.20 .11	0.88 .10	27.60
2008 Mar 4.2	+30.7	0.055	4.52	27.76 .00	25.58 .01	25.16 .00	24.66 .01	25.32 .00	1.76 .05	1.67 .03	1.54 .03	27.87
2008 Mar 4.2	+30.7	0.055	4.33	27.76 .01	25.59 .01	25.14 .00	24.61 .01	25.29 .00	1.67 .06	1.57 .04	1.65 .03	27.86
2008 Mar 5.2	+31.7	0.057	4.43	27.72 .01	25.55 .01	25.12 .00	24.60 .01	25.27 .00	1.64 .06	1.52 .05	1.56 .03	27.83
2008 Apr 30.2	+87.8	0.188	4.61	27.04 .06	25.15 .10	24.72 .03	24.22 .09	24.81 .03	1.36 .40	1.26 .20	1.18 .18	27.08
2018 Oct 6.3	-67.6	0.139	4.19	27.31 .03	25.15 .04	24.65 .05	24.21 .04	24.80 .01	0.80 .38	1.34 .05	1.26 .05	27.37
2018 Oct 6.3	-67.6	0.139	4.51	27.27 .02	25.17 .02	24.66 .02	24.27 .02	24.81 .01	1.00 .25	1.25 .05	1.24 .05	27.33
2018 Oct 6.3	-67.6	0.139	3.89	27.33 .04	25.18 .05	24.66 .02	24.11 .03	24.79 .01	1.33 .13	1.41 .04	1.42 .04	27.39
2018 Oct 6.3	-67.6	0.139	4.19	27.27 .02	25.13 .04	24.65 .02	24.19 .02	24.79 .01	1.17 .18	1.31 .04	1.30 .04	27.34
2018 Nov 7.2	-35.7	0.064	4.25	27.69 .01	25.49 .01	24.97 .00	24.55 .01	25.13 .00	1.47 .05	1.57 .01	1.53 .01	27.79
2018 Nov 7.3	-35.7	0.064	3.93	27.69 .01	25.51 .01	24.97 .00	24.50 .01	25.13 .00	1.62 .04	1.62 .01	1.62 .01	27.79
2018 Nov 7.3	-35.7	0.064	3.63	27.68 .02	25.52 .02	24.97 .01	24.50 .01	25.12 .00	1.49 .05	1.67 .01	1.66 .01	27.78
2018 Nov 7.3	-35.6	0.064	3.93	27.70 .01	25.52 .01	24.97 .01	24.51 .01	25.13 .00	1.51 .05	1.63 .01	1.59 .01	27.81
2018 Nov 15.3	-27.7	0.049	4.05	27.76 .01	25.56 .01	25.01 .00	24.57 .00	25.16 .00	1.41 .04	1.67 .01	1.66 .01	27.87
2018 Nov 15.3	-27.7	0.049	3.54	27.74 .02	25.56 .01	25.00 .01	24.52 .01	25.15 .00	1.53 .03	1.69 .01	1.69 .01	27.85
2018 Nov 15.3	-27.6	0.049	3.84	27.74 .01	25.55 .01	25.00 .00	24.54 .00	25.15 .00	1.51 .03	1.66 .01	1.65 .01	27.85
2018 Nov 15.3	-27.6	0.049	4.05	27.74 .01	25.55 .01	25.00 .00	24.56 .00	25.15 .00	1.44 .04	1.61 .01	1.61 .01	27.85
2018 Nov 15.3	-27.6	0.049	3.84	27.75 .02	25.55 .01	24.99 .00	24.53 .01	25.15 .00	1.53 .04	1.66 .01	1.63 .01	27.86
2018 Dec 3.1	-9.8	0.027	3.59	27.80 .01	25.64 .01	25.08 .00	24.59 .00	25.25 .00	1.72 .01	1.80 .00	1.78 .00	27.92
2018 Dec 3.1	-9.8	0.027	3.92	27.78 .00	25.64 .00	25.08 .00	24.62 .00	25.26 .00	1.69 .01	1.77 .00	1.75 .00	27.90
2018 Dec 3.1	-9.8	0.027	3.29	27.79 .01	25.64 .01	25.06 .00	24.58 .00	25.23 .00	1.71 .01	1.80 .01	1.80 .01	27.91
2018 Dec 3.1	-9.8	0.027	3.80	27.78 .00	25.64 .00	25.08 .00	24.61 .00	25.25 .00	1.70 .01	1.79 .00	1.76 .00	27.90
2018 Dec 3.1	-9.8	0.027	3.71	27.78 .00	25.64 .00	25.07 .00	24.59 .00	25.25 .00	1.71 .01	1.80 .00	1.77 .00	27.90
2018 Dec 3.2	-9.8	0.027	3.50	27.79 .00	25.63 .01	25.08 .00	24.60 .00	25.24 .00	1.71 .01	1.80 .00	1.79 .00	27.91
2018 Dec 3.2	-9.8	0.027	3.40	27.76 .01	25.60 .01	25.05 .00	24.57 .00	25.22 .00	1.72 .01	1.80 .00	1.79 .00	27.88
2018 Dec 3.2	-9.8	0.027	3.19	27.78 .01	25.62 .01	25.07 .00	24.57 .00	25.22 .00	1.73 .01	1.81 .01	1.82 .01	27.90
2018 Dec 3.2	-9.8	0.027	2.99	27.76 .01	25.59 .01	25.06 .01	24.56 .01	25.20 .01	1.73 .01	1.81 .01	1.81 .01	27.88
2018 Dec 3.2	-9.7	0.027	3.29	27.76 .01	25.61 .01	25.08 .00	24.59 .00	25.22 .00	1.71 .01	1.79 .00	1.81 .01	27.88
2018 Dec 3.2	-9.7	0.027	3.59	27.75 .00	25.64 .00	25.07 .00	24.59 .00	25.23 .00	1.69 .01	1.80 .00	1.79 .00	27.87
2018 Dec 3.3	-9.7	0.027	3.59	27.77 .00	25.63 .00	25.07 .00	24.59 .00	25.23 .00	1.67 .01	1.79 .00	1.79 .00	27.89
2018 Dec 16.3	+3.3	0.024	3.43	27.73 .00	25.59 .00	25.09 .00	24.60 .00	25.23 .00	1.99 .00	2.06 .00	2.08 .00	27.85
2018 Dec 16.3	+3.4	0.024	3.64	27.72 .00	25.61 .00	25.08 .00	24.60 .00	25.24 .00	1.98 .00	2.05 .00	2.05 .00	27.84
2018 Dec 16.3	+3.4	0.024	3.13	27.74 .00	25.59 .01	25.05 .00	24.56 .00	25.22 .00	1.98 .00	2.05 .00	2.07 .00	27.86
2018 Dec 16.4	+3.4	0.024	3.64	27.75 .00	25.62 .00	25.08 .00	24.59 .00	25.24 .00	1.99 .00	2.06 .00	2.07 .00	27.87
2018 Dec 30.1	+17.1	0.034	3.60	27.65 .01	25.52 .01	25.03 .00	24.51 .00	25.17 .00	1.81 .01	1.88 .00	1.86 .00	27.77
2018 Dec 30.1	+17.2	0.034	3.92	27.64 .00	25.53 .00	25.04 .00	24.53 .00	25.19 .00	1.76 .01	1.83 .00	1.82 .00	27.76
2018 Dec 30.1	+17.2	0.034	3.30	27.66 .01	25.53 .01	25.04 .00	24.50 .00	25.17 .00	1.80 .01	1.88 .00	1.87 .01	27.78
2018 Dec 30.1	+17.2	0.034	3.60	27.63 .00	25.50 .00	25.02 .00	24.51 .00	25.17 .00	1.78 .01	1.85 .00	1.84 .00	27.74
2019 Jan 31.2	+49.2	0.094	4.03	27.35 .00	25.25 .01	24.83 .00	24.28 .01	24.95 .00	1.53 .02	1.59 .01	1.57 .01	27.44
2019 Jan 31.2	+49.3	0.094	4.36	27.35 .00	25.23 .01	24.84 .00	24.31 .01	24.98 .00	1.56 .02	1.54 .01	1.51 .01	27.43
2019 Feb 26.2	+75.2	0.157	4.27	27.04 .01	24.85 .04	24.60 .01	24.09 .02	24.69 .01	1.05 .15	1.38 .04	1.34 .04	27.10
2019 Feb 26.3	+75.3	0.157	4.27	27.04 .01	24.85 .03	24.60 .01	24.06 .02	24.68 .01	1.37 .07	1.31 .04	1.11 .07	27.09
2019 Mar 25.2	+102.2	0.221	4.28	26.69 .02	24.16 .24	24.41 .02	23.82 .06	24.49 .04	1.31 .15	1.02 .16	1.19 .11	26.71
2019 Mar 25.2	+102.3	0.221	4.47	26.75 .01	24.61 .10	24.41 .02	23.91 .05	24.49 .03	1.11 .23	1.07 .14	1.02 .16	26.77

^a Production rates and $A(\theta)f\rho$ followed by the upper, i.e. the positive, uncertainty. The “+” and “-” uncertainties are equal as percentages, but unequal in log-space; the “-” values can be computed.

^b “*und*” stands for “undefined” and means the continuum flux was measured but was less than 0.

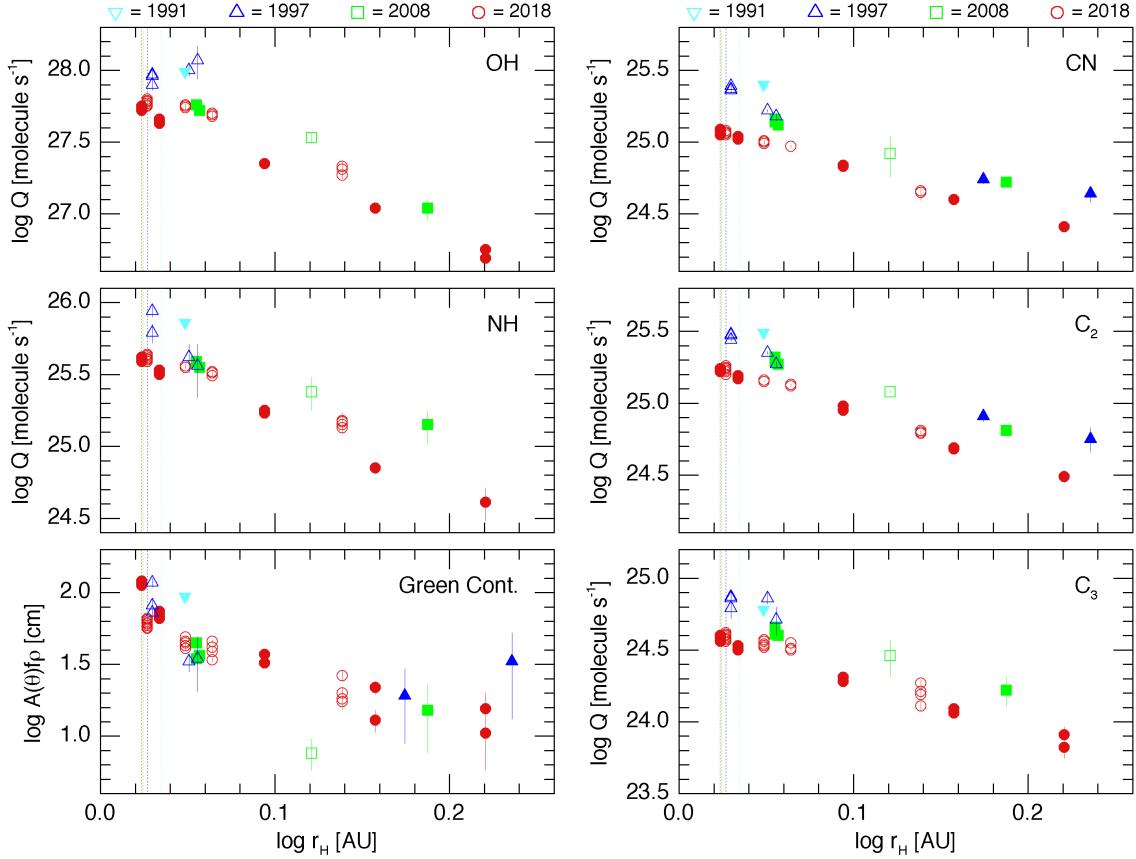


Figure 1. Logarithm of the production rates for observed molecular species and $A(\theta)f\rho$ for the dust as a function of the logarithm of the heliocentric distance. The species is indicated in the upper right of each plot. Different symbols are used for each apparition and are given above the plots; open points are pre-perihelion and filled points are post-perihelion. Error bars are plotted for all points; in some cases they are smaller than the symbols and are therefore not visible. Aperture sizes and other relevant parameters are given in Tables 2–4.

2018, for a total decrease of about 60%. C_2 and C_3 are similar, decreasing by totals of about 53% and 46%, respectively. Due to the pre-/post-perihelion asymmetries previously noted for OH and NH, the secular trends are somewhat suppressed, but yet are still $\sim 51\%$ and $\sim 53\%$, respectively. This factor of two or more decrease is the second largest that we’ve measured within our entire photometry database of more than 190 comets (Schleicher & Bair 2016), exceeded only by 103P/Hartley 2 – another hyperactive object having only recently had its perihelion distance substantially decreased.

3.3. Dust Behavior

The nominal $A(\theta)f\rho$ values for the green continuum shown in the lower-left panel of Figure 1 exhibit much more apparent scatter than do the molecular species because of two reasons – phase angle effects and significant aperture trends – that must be corrected in order to investigate the underlying behavior of the dust grains.

As is often the case for the dust in comets, there is a clear downward trend in the derived $A(\theta)f\rho$ values with increasing aperture size, which has in the past been attributed to some type of fading grains, likely either due to grains becoming darker or shrinking in size with time as they coast away from the nucleus (cf. Baum et al. 1992).

Accounting for this aperture effect is particularly important due to the very wide range in aperture sizes employed during the 2018/19 apparition associated with the very close approach of Wirtanen to the Earth. Fortunately, the characteristics of this aperture effect were consistent during the apparition. We, therefore, used a multi-step procedure to adjust all $A(\theta)f\rho$ results to a normalized aperture radius of 10^4 km. Because our best sampling took place on December 3, with 12 observational sets over nine different apertures, we used that night’s results of $\log A(\theta)f\rho$ vs $\log \rho$ as our fiducial. We then adjusted the data from each other night up or

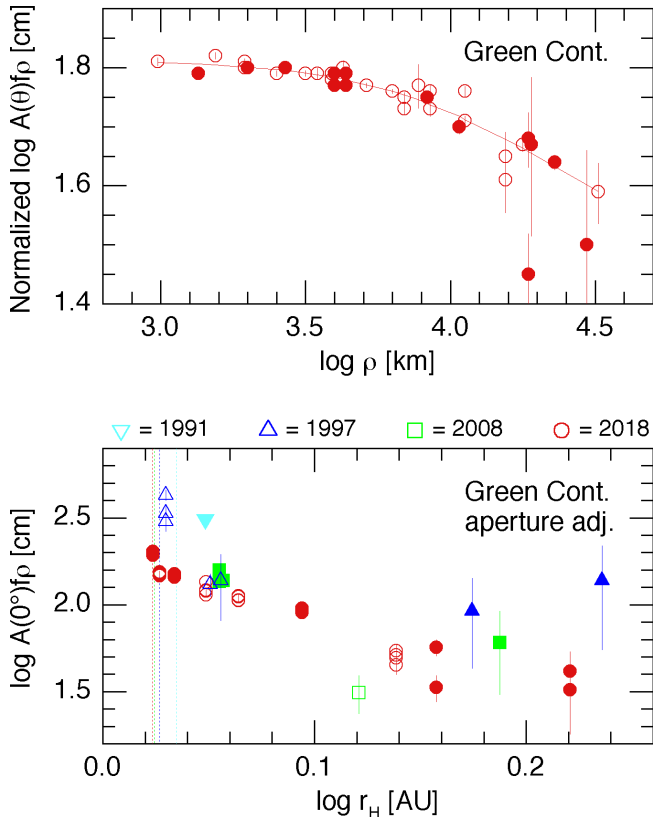


Figure 2. *Top:* Logarithm of normalized $A(\theta)f\rho$ for the dust as a function of the logarithm of the aperture radius for the 2018/19 apparition. *Bottom:* $A(0^\circ)f\rho$ for the dust as a function of the logarithm of the heliocentric distance. Symbols for both panels are as given in Figure 1. The curve in the top panel is the composite aperture adjustment described in the text.

down in log space to best overlay the December 3 data, ultimately yielding the compound aperture curve shown in the top panel of Figure 2. This curve was then re-normalized at 10^4 km, and each original $A(\theta)f\rho$ result was adjusted appropriately. Because the measurements at earlier apparitions generally were made with much larger projected aperture sizes due to Wirtanen’s much larger geocentric distances, we also applied a first-order aperture correction to these $A(\theta)f\rho$ results, simply using a near-linear (in log space) extrapolation of the aperture correction curve just discussed, again normalizing to 10^4 km.

We next applied our standard correction for phase angle effects (cf. Schleicher & Bair 2011), normalizing to 0° phase angle (the phase adjustment for each night is given along with the phase angle in Table 2). The results, after applying both adjustments, are shown in the bottom panel of Figure 2. The r_H -dependence (-3.8) for 2018/19 is most similar to that of C_2 , discussed previously. It is clear that there has also been a major

decrease in dust production, by more than a factor of two, from the 1990s to the past dozen years, though possibly not at the same rate of change from orbit to orbit as for the gas species. This last conclusion is uncertain, however, due to its dependence on the aperture extrapolation for large aperture sizes noted above.

The color of the dust grains, based on the green and UV continuum data, is unexceptional, with a mean value of $\Delta\log(A(0^\circ)f\rho)$ of ~ 0.09 , while the green minus blue value is about -0.01 ; each is somewhat below usual. We also detect a very small trend in color with aperture size. Note however, that the low dust-to-gas ratio in Wirtanen, discussed next, implies the possibility of residual contamination of the continuum bandpasses by various gas emissions, even following our standard decontamination procedures. Our experience with the entire photometry database suggests that both the more neutral colors and the slight aperture trend in colors could readily be due to contaminations, and we therefore do not pursue colors further.

The mean log dust-to-gas ratio, based on $\log[A(0^\circ)f\rho] - \log Q(\text{OH})$, is -25.55 cm s molecule $^{-1}$, only about one-quarter of the phase adjusted value in comets 1P/Halley, 81P/Wild 2, and 67P/Churyumov-Gerasimenko, or one-half the value in 9P/Tempel 1, i.e., somewhat less dusty than comets explored by spacecraft but not at all unusual; for instance it is $15\times$ greater than the extreme case of 2P/Encke (Schleicher & Bair 2016).

3.4. Water Production and Effective Active Area

Using our empirical conversion from a Haser OH production rate to the equivalent vectorial water production rate (cf. Cochran & Schleicher 1993; Schleicher et al. 1998), we obtain the values listed in the final column in Table 4. With a factor of $r_H^{0.5}$ in the conversion, the final slopes are 0.5 steeper than the values listed for OH above. Given the observed asymmetry about perihelion, it is not surprising that the peak value for water, 8×10^{27} molecules s $^{-1}$, was measured on December 3 ($\Delta T = -10$ day) rather than on our next night of photometry of December 16. Using a water vaporization model based on the work of Cowan & A’Hearn (1979, with a factor of two error corrected, M. A’Hearn 2010 private communication), this peak value corresponds to an effective active area of about 2.5 km 2 . Combined with an effective nucleus radius of 0.6 km (Lamy et al. 1998; consistent with radar estimates, E. Howell, priv. comm.), one obtains an active fractional area of about 55%, as compared to a corrected value of about 80% in 1997 (Farnham & Schleicher 1998). There are several caveats, however, regarding this value. First, the area and active fraction are significantly smaller than this

at larger heliocentric distances because of the steep r_{H} -dependence; at the furthest point out-bound, the values drop to only one-fifth of the peak values. Second, the imaging results strongly suggest that some, if not the majority, of the water is coming off of the nucleus as icy grains (see next section). In this case, the source regions could be significantly smaller than areas computed with the vaporization model. Finally, the peak values in the 1990s slightly exceed the nominal total surface area of 4.5 km^2 , further suggesting an icy grain component for the observed water.

A comparison of water production rate determinations by various investigators for the 1997 apparition, when Wirtanen was the planned *Rosetta* target, has already been performed by Fink & Combi (2004). As they discussed in detail, there is considerable scatter among the various datasets but most of this apparent disagreement is a result of investigators using differing values for Haser scalelengths. The most extensive dataset, both during 1997 and most subsequent apparitions, was obtained using the SWAN instrument on *SOHO* as recently summarized by Combi et al. (2020). In addition to the only measurements during the 2002 apparition, they also obtained data in 2008 and 2018. Besides using very different techniques, with SWAN measuring the very large hydrogen Lyman- α coma while we measure the inner OH coma, the cadence of observations greatly differs. While SWAN’s brightness threshold permits only a small range of heliocentric distances to be covered, it can often obtain near-daily measurements when the comet is within range. Thus, our r_{H} -dependent slopes are more robust while SWAN can be used to identify outbursts. Keeping these aspects in mind, we refer to Figure 2 in Combi et al. (2020) where there is a very large dispersion among their measurements during the 2002 apparition. In fact, only five of the 28 data points might be considered baseline activity and very close to the 1997 values, while the remaining are as much as $5\times - 6\times$ higher and appear to be associated with several sustained outbursts. In 2008 we have no overlap in datasets, as ours are all at larger distances than the SWAN data, though an extrapolation of our values is in reasonable agreement.

Of the five nights near perihelion for which we have data close in time with the SWAN results, we start somewhat higher in mid-November, are quite close in early-December, about 10% low in mid- and late-December, and quite close at the end of January, though comparisons are inexact due to night-to-night variations in the SWAN data (Combi et al. 2020, see their Figure 2). We conclude that our agreement is quite good overall, despite sometimes large differences in derived r_{H} -dependencies between our values and theirs that we at-

tribute to our generally having much wider ranges of heliocentric distance. In particular, we note that they found that water production in Wirtanen dropped by about a factor of two between 1997 and 2018, essentially identical to our own findings.

4. IMAGING RESULTS

In contrast to our just discussed photometry which spanned multiple apparitions, our imaging covered only the 2018/19 apparition, but with many more epochs of observations in order to glean as much information as possible out of the rapidly varying viewing geometry. As is evident from Table 1, the majority of our imaging nights consisted of only CN and broadband R or r' (to monitor dust) images. This was the result of several factors. OH, NH, and C_3 are fainter than CN, and OH and NH are subject to significant atmospheric extinction that limits their observability to only very low airmasses. Furthermore, NH, C_2 , and C_3 suffer dust contamination that required photometric conditions in order to be properly analyzed, and such calibrations were too time consuming except on our dedicated nights. We made a programmatic decision to prioritize regular CN monitoring from December onwards so that we could tightly constrain the rotation period at as many epochs as possible to look for a changing rotation period; this strategy has proven to be very successful in the past, e.g., for C/2004 Q2 Machholz (Farnham et al. 2007), C/2007 N3 Lulin (Bair et al. 2018), 103P/Hartley 2 (Knight & Schleicher 2011; Samarasinha et al. 2011), and 41P/Tuttle-Giacobini-Kresák (Schleicher et al. 2019). The CN imaging was the focus of Paper I; below we concentrate on the morphology and behavior of the dust and the remaining gas species.

4.1. Dust Morphology and Behavior

Although our imaging emphasis throughout the apparition was on the gas species, we obtained frequent broadband R or r' images since they have minimal gas contamination, making them a high signal-to-noise proxy for a pure dust image. Narrowband continuum filters were used on many photometric nights and confirmed the validity of this approach, so we will henceforth refer to R or r' images as “dust” images. We nearly always paired dust images with CN images, meaning that we have a robust dataset for searching for rotational variation in the dust as well as the gas coma.

Throughout the apparition, dust images were brighter in the anti-sunward hemisphere, with the brightness concentrated in the expected tailward direction (see the top row of Figure 3). The general shape evolved slowly as the viewing geometry changed, but did not change appreciably on shorter, e.g., rotational, timescales. We did

not detect any fainter, time-varying features analogous to the gas jets (discussed in Paper I and the following subsection), despite analyzing the dust images with the same enhancement techniques. However, we note that we generally ignore features within a few PSFs of the center in enhanced images since this region is most susceptible to processing artifacts; any real and varying dust features, if they exist, likely extend less than ~ 5 arcsec, or $\lesssim 1000$ km. The lone exception occurred on December 16 and 17, when a persistent feature appeared very close to the nucleus. We attribute this to either slow moving dust from the December 12 outburst (Farnham et al. 2021) or to a quirk of the viewing geometry; see Section 5.6 for further discussion.

The lack of an obvious rotational signature in the dust is both expected and surprising. On the one hand, we have detected time-varying jet-like features in CN in many comets brighter than $V \sim 13$ and within ~ 1 AU of Earth over the years with only a few, e.g., C/1996 B2 Hyakutake (Schleicher & Woodney 2003) and 103P/Hartley 2 (Knight & Schleicher 2013), exhibiting rotational variation in the dust, so the lack of rotation signature in Wirtanen is not surprising. On the other hand, we have generally assumed that such features are not seen, in part, because the dust has low ejection velocities and large velocity dispersions, requiring excellent spatial resolution to be identified. We have also frequently seen approximately stationary sunward-facing features in some comets, e.g., C/2007 N3 Lulin (Bair et al. 2018), 41P/Tuttle-Giacobini-Kresák (Bair et al. 2018; Schleicher et al. 2019), yet such features are absent in Wirtanen. Wirtanen’s historically close apparition should have made the identification of any such features far easier than in most comets.

There is a faint, but noticeable, asymmetry in the bulk dust brightness which favors the hemisphere in which the carbon-bearing gases (CN, C₂, and C₃) are brightest. This is most obvious in Figure 3 on December 13 and 16, where these gases are brightest to the southeast, and the dust images are clearly brighter to the southeast than to the northwest. We attribute this asymmetry to the majority of the dust originating from the same source regions as the gases before being pushed tailward by radiation pressure. We will further explore the ties between the dust and gas in Section 6.

4.2. Gas Morphology

We obtained images of sufficient quality to assess the gas morphology in November (CN, C₃, C₂), December (OH, NH, CN, C₂, and C₃), January (OH, CN), and February (CN). Representative pure gas images following continuum subtraction as well as a BC (dust) im-

age on five nights are shown in Figure 3. These images have all been enhanced by subtraction of an azimuthal median (cf. Schleicher & Farnham 2004; Samarasinha & Larson 2014); the CN morphology differs somewhat from images at the same times shown in Paper I because in that paper we removed a temporal average to enhance the images. Temporal averaging requires evenly spaced images in rotational phase of similar quality and with minimal intervening change in viewing geometry. As there were insufficient images of any other gas species to construct the needed temporal average, we have opted to show all images here with the same enhancement technique for direct comparison. As discussed in Paper I, the temporal average enhancement made faint features in the darker half of the image more evident; without this enhancement here we cannot comment on the existence of such features in OH, NH, C₂, or C₃.

An additional difference in appearance relative to Paper I is our removal of underlying dust continuum when possible. The amount of underlying continuum varies from species to species (cf. Farnham et al. 2000), but is increasingly less important at larger distances from the nucleus since dust brightness falls off much more rapidly than does gas brightness. As described in the previous subsection, throughout most of the apparition the only distinct dust feature was the tail. This provided a convenient way to check that the continuum removal worked as intended, since over- or under-removal would result in negative or positive tail signatures remaining in the gas images, respectively. The only potential concern is the broad OH and NH morphology which mostly overlaps the continuum. However, in both cases the gas lacks an obvious increase in brightness overlapping the tail. As the tail is much brighter than the bulk brightness at comparable distances from the nucleus, its signature should be evident in the “pure” gas images if our calibrations had gone awry. We can be confident in our assessments of the gas jets described below since these do not appear in the continuum and are unlikely to be an artifact of the calibration process.

Since CN had the highest signal-to-noise on all nights, we use it as our fiducial for comparison to the other species. The CN morphology gradually evolved during the apparition as described in detail in Paper I and shown in their Figures 3 and 6. We briefly summarize it here to provide the context for the other species that did not have comparable temporal coverage. There were two obvious CN jets seen during the apparition, one that persisted throughout a rotation and one whose brightness was more strongly modulated. The morphology progressed from a face-on spiral rotating in the clockwise direction in November to a broad, edge-on spiral with

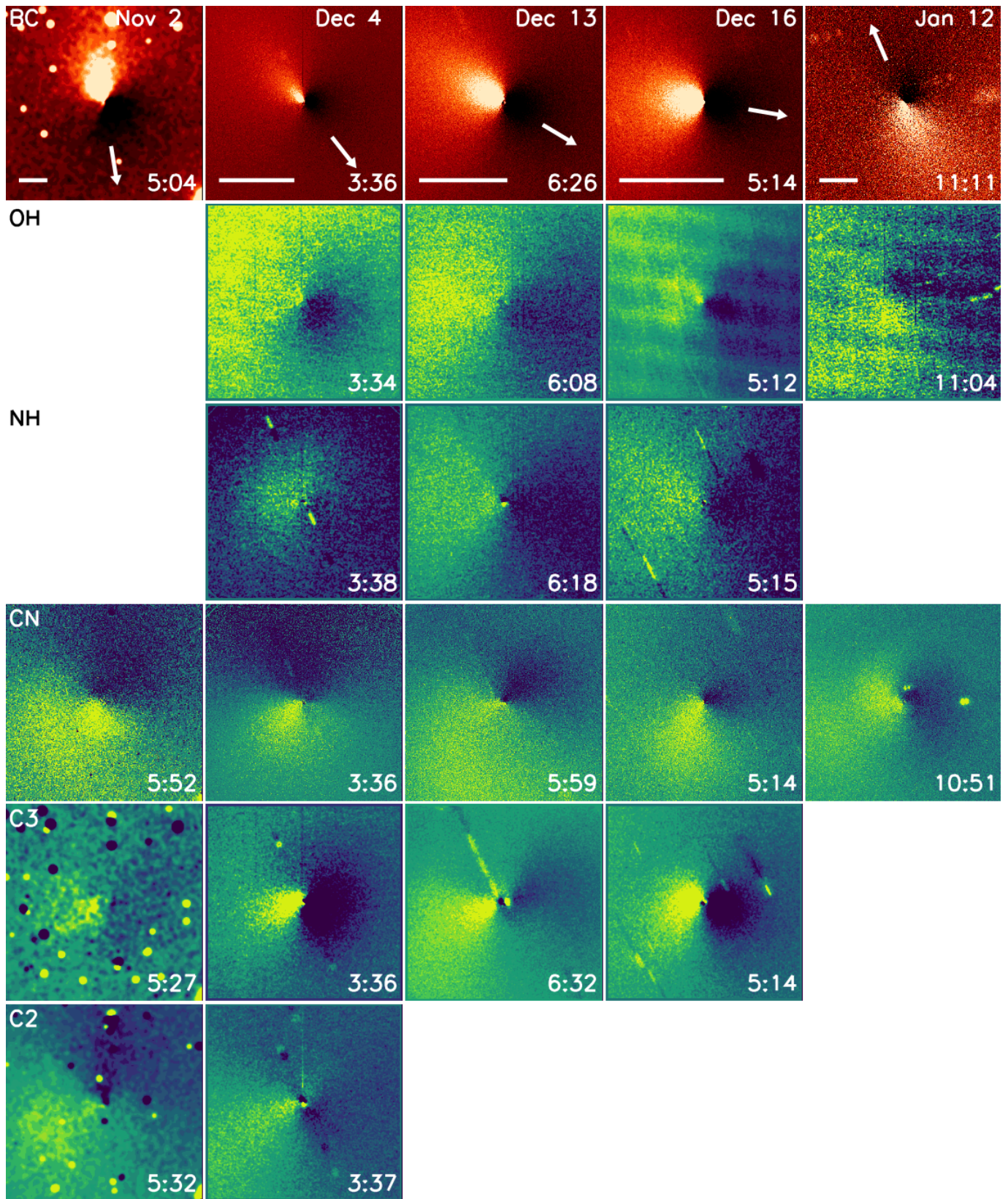


Figure 3. Morphology of dust and pure gas species at five different epochs. The species shown on a given row is labeled in the first column, and the date of a given column is displayed in the top panel. Image mid-times are in the bottom right corner. All images are centered on the nucleus with north up and east left, and have been enhanced by division of an azimuthal median. A 5000 km scale bar and the direction to the Sun are indicated on the top row for each night. Trailed stars can be seen in many images; positive (yellow) are stars in the gas image while negative (blue) are stars in the continuum image that was removed. Faint vertical lines are seen in some panels due to a bad column on the LMI detector, while the regular, cross-hatched pattern in the OH panels is due to the construction of the CCD which becomes visible in faint UV images.

hints of a corkscrew structure and little variation with rotational phase for most of the rotation cycle in mid-December, to a face-on spiral with the reverse sense of rotation (i.e., counter-clockwise) by January. The morphology evolution will be further revisited in the next section as a modeling constraint.

As also discussed in Paper I and shown in their Figure 6, the CN morphology repeated with a period of ~ 9 hr, with the period first increasing then decreasing during the apparition. For the following comparisons we have chosen the CN image whose midpoint is closest in time to the other species being considered. Since the gas images presented here were generally median combinations of 3–5 images, and some nights’ images were acquired sequentially while others were interspersed, the mid-times are sometimes within a minute of a CN frame, while on other nights, they differ by up to 45 minutes. Even in the most extreme case, the temporal separation is relatively small compared to the period of repetition and does not affect our interpretation. Furthermore, given the high-fidelity of our model (Section 5) to replicate the CN morphology throughout the entire apparition, we can confidently predict what the CN morphology would have been at the time of another image as an additional check.

4.2.1. Carbon-bearing species: CN, C₂, and C₃

CN, C₂, and C₃ exhibit similar morphology when acquired contemporaneously, as can be seen in Figure 3. On 2018 November 2 (first column) no jet is discerned, but all three are brightest in the southeast quadrant. On December 4, 13, and 16 (middle three columns), all three species have a dominant feature leaving the nucleus at a position angle (P.A.) measured from north through east around $120^\circ - 135^\circ$. Neither C₂ nor C₃ was obtained after 2018 December, so they are not seen in the final column. Although we only show one set per night, multiple sets were acquired on some nights and the C₂ and C₃ morphology varied in a similar manner to the CN from set to set. We thus conclude that all three carbon-bearing species originate from the same source regions, a conclusion supported by their similar production rate r_H -dependencies and explored further in Section 6.

Although the general appearance and locations of features are similar across CN, C₂, and C₃, they are not identical for several reasons. None of the three species is considered to be a “parent” volatile; they do not sublimate directly from the ice on the nucleus, but instead arise as a second generation (“daughter”) or third generation (“grand-daughter”) produced via photodissociation or chemical processes. The parent(s) or grandparent(s) of the three species are not well constrained,

but CN and C₂ are likely primarily daughter species from several parents, while C₃ (and C₂ to some extent) may be produced by chemical reactions in the coma (cf. Helbert et al. 2005). The combination of different formation pathways with different lifetimes – C₃ has a Haser scale length roughly an order of magnitude shorter than CN and $2.4\times$ shorter than C₂ (cf. A’Hearn et al. 1995) – results in different spatial distributions for each species. These natural differences in morphology are further muddled by the non-simultaneity of some images and, as will be shown in Section 5, the fact that the primary feature we see varying in December is actually composed of two wide, overlapping jets.

4.2.2. OH and NH – Products of icy grains?

OH and NH exhibit similar morphology to each other, although the NH data are relatively limited, and both are different from that of the carbon-bearing species. We were not able to make an assessment in 2018 November as the signal-to-noise of OH was too low and NH was not acquired. As shown in the second through fifth columns of Figure 3, OH and NH both exhibited a roughly hemispheric brightness enhancement in the direction of the dust tail (shown in the BC row) and lacked any well-defined jets as seen in CN, C₂, and C₃. There was no evidence of variation with rotational phase for either OH or NH on any of these nights.

The rotational variation of CN was discussed thoroughly in Paper I, but we revisit it briefly here to further illustrate the invariance of OH. We obtained CN images with a ~ 45 minute cadence for 9–11 hours on 2019 January 26 and 28 as well as OH images every ~ 45 min for ~ 5 hours on the same nights. The temporal coverage and spacing ensure a full rotational cycle for CN was sampled each night; when both nights are phased together we also have a complete OH rotational cycle, and repetition of CN morphology from night to night confirms the validity of this combination. As shown in Figure 4, CN evinces a pinwheel shape, with one or two jets visible and rotating counter-clockwise throughout the night, and the bulk brightness is always primarily to the east. The OH shows no variation, but is always brightest towards the south on this night, in the general direction of the tail.

The OH and NH morphology and lack of rotational variation are consistent with these gases being released from icy grains in the coma. Icy grains containing OH and NH (or more likely their parent molecules) released from the nucleus would be swept tailward due to radiation pressure, and the excess velocities in random directions imparted during photodissociation, coupled with long lifetimes, would result in a much broader dis-

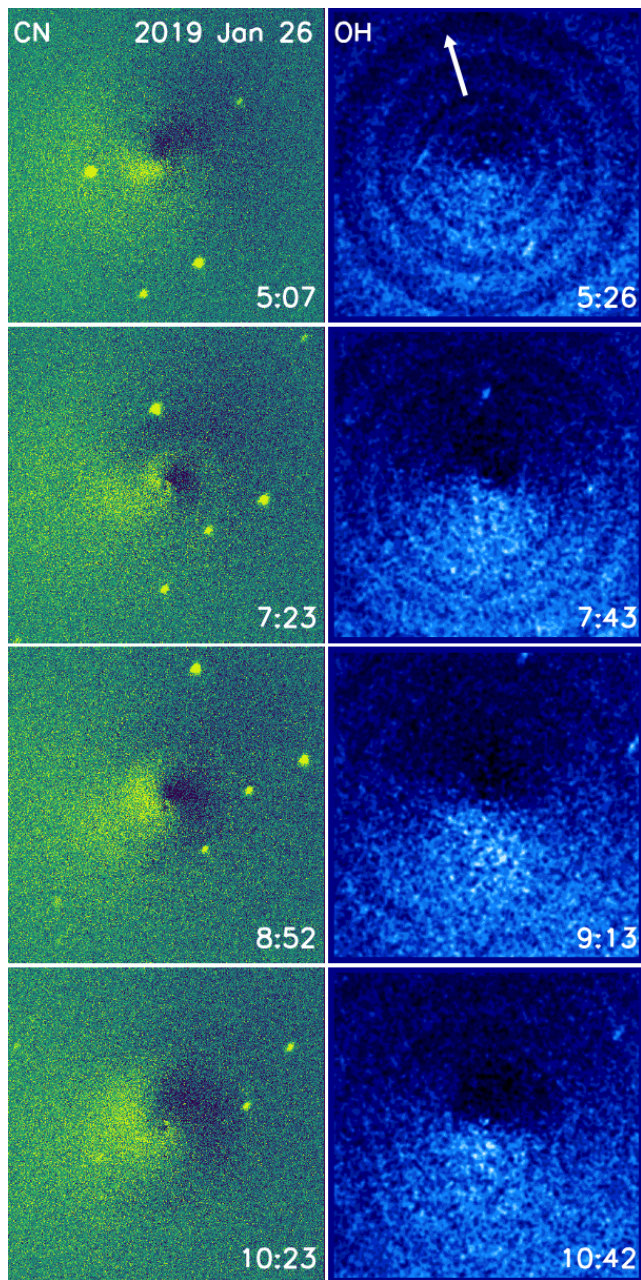


Figure 4. Comparison of CN and OH throughout one night (2019 Jan 26). CN images are plotted in the left column, OH in the right column. Image mid-times are given on each panel. All images are 60,000 km across at the comet, are centered on the nucleus, have been enhanced by subtraction of an azimuthal median, and are aligned with north up and east to the left. Trailed stars can be seen in some CN frames, while the ring-like structures seen in some OH panels are artifacts of the enhancement.

tribution of the resulting OH and NH than exhibited by the dust tail. Icy grains have long been hypothesized as existing in the comae of some comets (e.g., A’Hearn et al. 1984). Their unequivocal detection by

EPOXI in 103P/Hartley 2 (A’Hearn et al. 2011; Protopapa et al. 2014) explained that comet’s hyperactivity, so their existence in Wirtanen, also considered hyperactive, was anticipated before the apparition. Surprisingly, icy grains were not detected in Wirtanen via IR spectroscopy (Protopapa et al. 2020). We observed similar dimorphism between OH & NH and the carbon-bearing species in Hartley 2 (Knight & Schleicher 2013) as reported here for Wirtanen, strengthening our confidence in the icy grain explanation. Although atmospheric extinction makes obtaining high signal-to-noise OH observations challenging for most comets, the utility of OH imaging for identifying icy grains is clear.

We hypothesize that the icy grains are released from the same source regions as the carbon-bearing species for several reasons. First, the OH and NH, like the dust, is somewhat brighter in the direction from which CN, C₂, and C₃ originate, as would be expected. The icy grains are presumably slow moving with large velocity dispersions, so any rotational signature is washed out, but the bulk brightness enhancement is preserved. Second, as will be discussed next, our modeling finds that the two source regions for the CN jets subtend $\sim 30\%$ of the surface, more than half of the 55% active fraction we find from photometry. If the remaining water (having an equivalent active fraction of $\sim 25\%$ of the nucleus) was released from other source regions, we’d expect some sort of morphological signature, but none is seen. Lastly, as discussed previously the production rates of all five gas species behaved generally similarly, suggesting they all originated from the same source regions. However, the steeper post-perihelion decrease in OH and NH than the carbon bearing species does suggest some compositional heterogeneity, to which we will return in Section 6.

5. MODELING THE CN JET MORPHOLOGY

5.1. Modeling Overview

Our Monte Carlo jet model has seen numerous enhancements since its early success in reproducing the dust jets observed in Comet Hyakutake (C/1996 B2; Schleicher & Woodney 2003). Most relevant here, we added the ability to vectorially apply the excess velocity of dissociation of a parent species to an observed daughter gas species, with the most recent example in our study of Comet Lulin (C/2007 N3; Bair et al. 2018). Since most aspects of the model are described in detail in these papers, we only briefly summarize other key aspects of the model. The model allows us to control the orientation and rotation rate of the nucleus, the size and location of multiple source regions, and their illumination function, as a function of time throughout an

apparition. While all computations are performed in the comet’s reference frame, a series of coordinate transformations yield the view as seen by the observer on Earth.

In practice, we incorporate a systematic top-down search of the multi-dimensional parameter space by first varying the parameters that determine the basic shape of an observed jet – pole orientation and source latitude – for representative images throughout the apparition. Viable solutions are further constrained by examining full rotational sequences. Because the apparent shape of spiral jets can change substantially as the width of the jet varies from narrow to broad, the entire process is repeated using several different widths. Only after converging on the comet’s pole orientation and each source location and size, are variations to other parameters investigated, such as the solar illumination function, outflow velocities, and the degree of dispersion from the radial direction. Finally, the values of all parameters are refined in an iterative process.

5.2. Basic Constraints for Comet Wirtanen

As noted in the Introduction, Comet Wirtanen’s 2018/19 apparition provided a nearly ideal set of circumstances for detailed monitoring of any morphological features in the inner coma over a wide range of viewing geometries. However, as will be seen, some of Wirtanen’s specific characteristics also provided several challenges during the process of modeling the observed jet morphology. We first itemize basic characteristics regarding Wirtanen’s physical properties that directly impact the subsequent modeling, some of which were already described and discussed. First, little to no variation was observed for the dust, and therefore only the CN gas images are used in the model. Fortunately, the typical high contrast of CN emission to the underlying continuum combined with Wirtanen’s relatively low dust-to-gas ratio, meant that there was no need to remove the continuum even quite close to the nucleus. Successive CN spiral features have similar brightnesses, shapes, and spacing, but subtle differences in an alternating pattern, thereby strongly suggesting two similar-sized source regions on opposite sides of the nucleus. The morphology is essentially identical from cycle to cycle and over multiple days, directly implying that there is no significant non-principal-axis rotation involved. Thus the ~ 9 hr periodicity requires that the sidereal period is also ~ 9 hr. To emphasize the extent of our dataset during this apparition, we plot the rotational phase coverage, as a function of time from perihelion for each set of CN images in Figure 5.

The CN features exhibit definitive clockwise rotation in the first-half of November, and counter-clockwise ro-

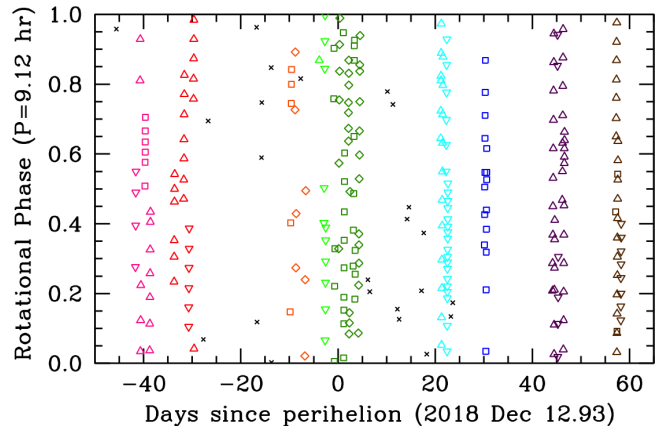


Figure 5. Rotational phase coverage of our CN images as a function of time from perihelion (ΔT) assuming a fixed sidereal rotation period of 9.12 hr. Squares and diamonds (on alternating nights to distinguish each night’s data) are observations obtained with the LDT, while triangles (up and down) are for 42-inch data. Each color represents an observing run, while black crosses indicate snapshot images from various telescopes (see Table 1). Because Wirtanen’s actual sidereal period varied significantly throughout the apparition, and only peaked at 9.14 hr in mid-December, this plot shows the distribution of observations in rotational phase space but not the actual rotational phases, which shift from run to run.

tation throughout January and early February; therefore, we must be viewing from opposite hemispheres at these times and the changeover occurred near closest approach. The shape of these features along with coarse modeling directly implies that the obliquity of the rotation axis was near 90° and that both source regions were near the equator. However, specific differences in the shapes of successive jets, particularly on the anti-sunward side both early and late in the apparition, with one jet showing face-on spirals and the other jet transitioning between face-on and side-on (i.e. corkscrew) spirals, implies the sources are centered at somewhat different latitudes. The features are always relatively round in shape and appear shell-like even as our view crossed the equator near closest approach during the jets’ transition from an apparent clockwise to counter-clockwise rotation, thereby requiring very broad jets. This characteristic also explains why a specific time for our passing through the plane of the jet is difficult to determine and why our line of sight seems to remain “within” the jet (in fact, both jets) for many days. Finally, the scale and outward motion of features imply that the bulk outflow velocity of the gas is $\sim 0.8 \text{ km s}^{-1}$.

5.3. Additional Issues and Complications

As described in Paper I, both the overall and specific appearance of the CN morphology can change greatly

depending on which enhancement methodology is used. With a strong sunward/anti-sunward asymmetry usually present, features on the anti-sunward side are often difficult to detect with the azimuthal average/median removal, but are readily evident using the temporal average removal since bulk features present throughout a rotational cycle are eliminated. While our model cannot directly replicate this latter enhancement method, it can crudely match the result by ignoring the solar illumination and allowing all particles to be emitted independent of the location of the Sun, thereby effectively removing the bulk asymmetry. Therefore, during our modeling we alternated between assuming a standard solar illumination function such as the cosine of the Sun’s zenith distance when attempting to match the actual brightnesses and this alternative when fitting features on the “night” side. Examples shown later in this section give the azimuthal average removal and temporal removal of representative images, along with the model solution using the solar function. As modeling progressed, it became obvious that indeed some gas is released even when the Sun is below the local horizon, but at a much reduced rate (roughly 10% of the rate when the Sun is at the zenith); this is included in the final model.

As noted, the shape of the features near perihelion need both jets to be very broad. Some aspects directly require that the source regions stretch over a large range of latitudes since the solar illumination function varies with latitude, while other aspects can be due to either a dispersion from the normal in the outflow direction and/or the amount of excess velocity in random directions when the CN parent dissociates. The latter in turn depends on the gas density and the collision rate – in the collisional zone, daughter molecules will be forced to continue to move radially outward, mimicking the Haser model, while beyond the collision zone the daughters will behave as expected from the vectorial model. Here, we assume a small amount of initial dispersion from the local normal direction (10° radius Gaussian) but, due to Wirtanen’s relatively low water production rate as compared to other comets that we’ve modeled, a higher than usual net excess daughter velocity (0.25 km s^{-1}). Note that these specific values are intertwined with the size of the source regions, and although this combination overall provides a good match of the entire coma brightness throughout the apparition, a moderate change in the value of one of these parameters can often be compensated for by an associated change in another of these parameters.

While Wirtanen’s broad and generally “soft” features increased the difficulty in performing our modeling, especially when attempting to match these features during

the rapidly changing viewing geometry in December, another, more serious complication was caused by Wirtanen’s changing rotation period. Our modeling confirmed the preliminary conclusion found in Paper I that the increase and subsequent decrease in Wirtanen’s apparent period was too large to be explained by synodic effects alone. Simply based on the pole constraints noted in the previous sub-section, the maximum offset between apparent and synodic periods could be no more than ~ 0.05 hr, whereas the apparent period changed by ~ 0.20 hr between mid-December and early February. A major consequence is that no single sidereal period could reproduce the morphology without causing large changes in source longitudes early and late in the apparition. As a practical aspect, since all calculations have the time of perihelion as the origin for temporal and longitudinal calculations, not knowing *a priori* the functional form of the changes in sidereal period meant that offsets accumulated over time. Ultimately, in an iterative process, we determined average sidereal periods between perihelion and each observing run necessary to prevent computed source longitudes from drifting over time. We return to the results from this process later in this section.

5.4. Constraints for Refining the Model Solution and Associated Results

During the overall iterative process of determining a final model solution, narrowing the range of viable pole orientations was a high priority. However, because of the large breadth of each jet, when we viewed the jets from a line of sight within, particles emitted from the extremes of the source region appeared to behave differently from the bulk of the particles. Thus the following is based both on the bulk characteristics of each jet as well as examining the shape and behavior of the extrema. As noted previously, in early November the jets clearly had an overall clockwise rotation, while in January the motion was counter-clockwise. Close examination revealed evidence of clockwise motion of the near-equatorial jet as late as during the December 3–6 run, and the opposite rotation by December 16–17. Combined, these suggest that the Earth crossed the equator, or the specific latitude of the center of the source region, about December 10–12. This, in turn, yields the principal angle of the pole (i.e., the perpendicular direction to the obliquity) of about $235\text{--}240^\circ$, and is nearly independent of the obliquity. Separately, the motion of features with rotation in early to mid-December was approximately north-to-south, with a P.A. of about $0\text{--}20^\circ$. These P.A.s near perihelion require that the obliquity was $<75^\circ$. By late January, the shapes of each jet place a lower limit on

the obliquity of $\sim 60^\circ$; thus, the obliquity of Wirtanen’s nucleus was most likely in the range of $65\text{--}70^\circ$. When combined with our final jet locations, our preferred solution, to the nearest 5° , had an obliquity of 70° and a principal angle of 240° in Wirtanen’s frame of reference. This directly corresponds to an R.A. of 319° and Declination of -5° and, due to our use of the righthand rule in the model, this is the direction of the positive or “north” pole.

To provide a crude check on the orientation of the comet’s spin axis, we turned to a basic technique that relies on measurements of coma features that reflect the apparent pole orientation (e.g., persistent linear jets or conical features centered around the spin axis). We have successfully used this technique to derive the pole orientations of a number of comets, including spacecraft targets where in situ data confirmed our results (e.g., Farnham & Cochran 2002; Farnham & Schleicher 2005; Schleicher 2006). Using the P.A. of the projected pole, we define a plane that contains the P.A. vector and the line-of-sight vector; the spin axis lies somewhere within this plane. Applying this process to different observations produces multiple planes, and if the viewing geometry changes sufficiently between the observations, then the intersection of the various planes reveals the orientation of the pole in three dimensions.

In the case of Wirtanen, we use the oscillating corkscrew shape observed to the east in early- and mid-December (Farnham et al. 2021). This feature is characteristic of a jet emanating from a source at mid-latitudes, with the radially outflowing gas producing a spiral-shaped cone as the nucleus rotates. When viewed from outside the cone, the spiral appears as an oscillating jet centered on the spin axis. Although this feature was seen only near perihelion, the viewing geometry changed dramatically ($> 40^\circ$) during that time, introducing ample parallax for the use of intersecting planes.

We can discern the corkscrew in observations from December 3, 9, 14 and 16, and in each case, we estimate the center of oscillation to lie at a P.A. $\sim 90^\circ$. Because of the diffuse nature of the broad jets, these are crude measurements with large uncertainties ($\pm 20^\circ$ on December 4 and 9, and $\pm 10^\circ$ on December 14 and 16). Using these P.A.s, we compute a best fit pole solution at R.A., Decl. = $141^\circ, +2^\circ$ with an uncertainty of $\sim 15^\circ$. The sense of rotation cannot be determined from the observations of the oscillating jet, so we cannot state whether this, or the 180° opposite solution ($321^\circ, -2^\circ$) is the positive pole. Figure 6 shows the projections of the derived planes onto the celestial sphere, with their intersections defining the pole direction. This solution compares favorably to the result derived from the de-

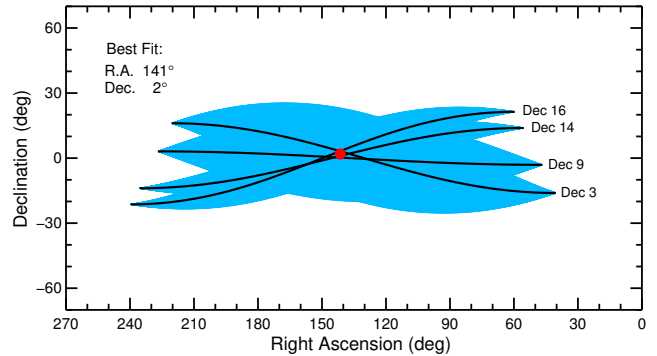


Figure 6. Pole solution showing the P.A./line-of-sight planes from the four observation dates, projected as great circles onto the celestial sphere. The intersection of the planes defines the pole orientation in three dimensions. The blue envelopes denote the uncertainties in each of the P.A. measurements. The best fit solution is given on the figure; as explained in the text, the exact opposite pole direction is an equally viable solution and agrees with our Monte Carlo modeling.

tailed modeling (if we accept that the corkscrew defines the negative pole), though the accuracy of the result, differing by only $\sim 4^\circ$, is probably somewhat fortuitous given the uncertainties in the measurements.

Having fixed our pole solution based on the modeling of the entire apparition, we could finalize the latitudes and the relative longitudes of the two source centers, along with their respective source radii. The primary, near-equatorial jet (shown in yellow in figures presented later in this section) is centered (to the nearest 5°) at a latitude of -5° and has a radius $>40^\circ$ with a best estimate of $\sim 50^\circ$. The secondary, “southern” jet (shown in green in figures presented later in this section) is centered at a latitude of -20° with a radius $>35^\circ$ and a best estimate of $\sim 40^\circ$. The secondary source is centered at a longitude $\sim 160^\circ$ greater than the primary source (with specific values tied to the sidereal period solution). Note that the center positions and the source sizes are somewhat interconnected as we needed to match either the presence or absence of material arising from the northernmost and southernmost parts of each source region. There is also some evidence that the secondary source is elongated approximately north-south, and may be somewhat narrower in longitude than in latitude. Also note that our modeling adopts a geocentric coordinate system, with emission normal to a spherical surface. Additional knowledge regarding the shape of the nucleus would be required to project these results back to their origins on a non-spherical topographic surface.

In addition to the requirements just discussed regarding source sizes and the need for reproducing features near the edges of the jets, another constraint came from

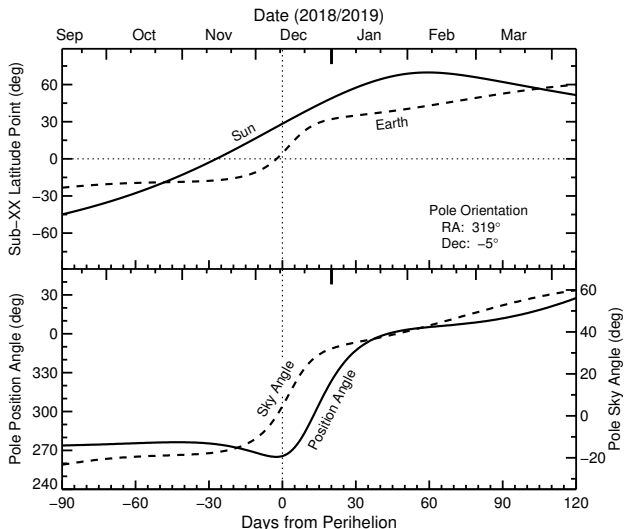


Figure 7. Sub-solar and sub-Earth latitudes plotted (top) as a function of time from perihelion, based on our preferred pole solution given in Table 5 from modeling the CN images. Note the near-steady increase in the sub-solar latitude (solid) until late in the apparition, while the sub-Earth latitude (dashed) varies rapidly during the few weeks surrounding closest approach to Earth (December 16). The orientation of the positive (“northern”) pole is plotted (bottom) as a pair of curves, with the P.A. of the projected pole (solid) and the projection angle from the plane of the sky (dashed).

the relative brightnesses of the two jets. In early November, they appeared nearly equally strong, while the primary jet dominates late in the apparition. As shown in the top panel of Figure 7, the sub-solar latitude varied substantially during the apparition, with a value of -49° only 100 days prior to perihelion, to -14° at the start of our imaging on November 1, to $+28^\circ$ at perihelion, $+50^\circ$ on January 3, and $+70^\circ$ at the end of our imaging on February 9. Thus the solar intensity favors the secondary source early on, but the southern portions of the secondary source would be continually in darkness late in the apparition. Based on these factors, in the final model, we assign 60% of the particles to the primary source, and 40% to the secondary source, for a 1.5:1.0 ratio, close to the simple ratio of areas of a 50° radius source as compared to a 40° radius region (1.53). These source sizes also correspond to about 18% and 12% of the total area of a spherical nucleus, significantly less than the nominal area required to match the water production rate, though the real fraction of the surface could be significantly different depending on the actual shape of the nucleus (see Section 3.4). However, as already discussed, OH imaging suggests that at least some of the water must be released as icy grains, providing a natural explanation for the apparent discrepancy.

Due to the very broad nature of the jets, the measured outflow velocity in the plane of the sky is nearly the same as the actual radial velocity. This is also directly associated with the round, shell-like appearance of the outward moving features near perihelion, similar to the planetary nebula effect (Samarasinha 2000; Schleicher & Farnham 2004). Ultimately, a near-constant parent outflow velocity of 0.76 km s^{-1} works very well throughout the apparition. We did not detect a decrease with heliocentric distance, but the change in distance was relatively small during our imaging (from 1.19 to 1.06 to 1.31 AU), and the poorer signal-to-noise prevented accurate jet measurements at larger r_H to look for reduced velocities. Including an assumed heliocentric dependence would not affect the modeling or interpretation due to the small distance range. While our value of 0.76 km s^{-1} is slightly smaller than calculations from early hydrodynamic models (cf. Combi et al. 2004), it is in good agreement with more recent modeling of low production rate comets (Shou et al. 2016).

5.5. The Changing Sidereal Period

Because all model calculations use perihelion as the fiducial and time from perihelion to compute the rotational phase for any given observation, we must know the “accumulated phase” throughout the apparition. While this is trivial when the rotation period is constant, it is very difficult when the period is changing in an unknown manner. A basic 4th order fit was made to the apparent periods determined in Paper I, and this worked well as an estimate of the instantaneous apparent period at any time from early November to early February. However, two complications arise for our modeling. First, all model calculations require the sidereal rather than the synodic or apparent period. Using our pole solution, the offset between these reaches a maximum at about +0.04 hr per rotation at closest approach to Earth (December 16) for the changing viewing geometry, while the offset due to the time from one local noon to the next on the comet reaches a maximum at about +0.02 hr per rotation approximately when the sub-solar latitude peaks (at $+70^\circ$) in early February (see Figure 8). How these affect the detailed jet morphology is quite complicated because projection effects are also varying throughout, but in all we expect the true sidereal period to match the apparent period in early November, to be $\sim 0.01\text{--}0.04$ hr per rotation less near perihelion/closest approach to Earth in mid-December, and be between $\sim 0.00\text{--}0.02$ hr per rotation less in early February. Thus, while the curve from Paper I provides an excellent guide as to the general changes in the sidereal period, one cannot simply apply an offset to this curve to obtain the correct curve to use for the sidereal period as a function of time.

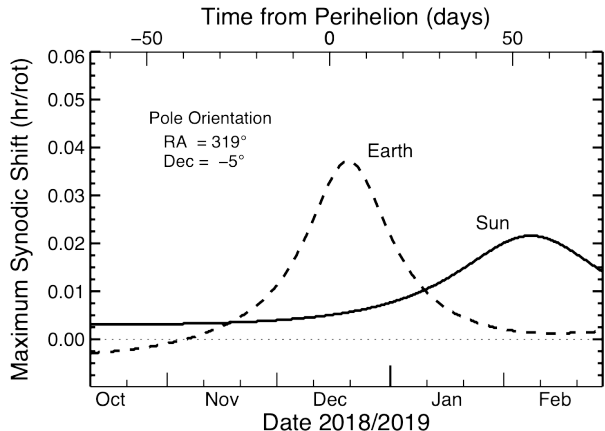


Figure 8. Nominal difference between the solar- (solid) and observer-based (dashed) components of the synodic, i.e., measured, period with the fundamental sidereal rotation period as a function of time around perihelion. The synodic shifts are calculated for a pole obliquity of 70° , as derived from our preferred pole solution (Table 5) from modeling of the CN images. The total offset between the apparent periods measured throughout the apparition are expected to be close to the combined values shown here, but other issues such as changing projection effects can slightly modify this.

The second complication arises in that any error in the sidereal period as a function of time will accumulate as one is further in time from perihelion. As an example, even only a small 0.01 hr per rotation offset or error grows to an accumulated offset of 1.50 hr by February 8, corresponding to $\sim 60^\circ$ longitude error for source region locations. Uncertainties associated with the detailed shape of the Paper I curve, especially near the extremes early and late in the apparition, coupled with the just noted estimated offsets between apparent and sidereal periods, makes it impractical to precisely determine the sidereal period for any particular observing run. Fortunately, we can partially mitigate this problem by forcing the source longitudes to remain fixed, but within the model this requires determining the average sidereal period for two dates – perihelion and the particular date of observation. When distinct morphological features are evident, as in early November and in early January to the end of our imaging, precise values for this average can be determined, and were used when making the final refinements. However, since even the rate of change in period over any particular interval is not tightly constrained, the specific sidereal period for any date cannot be precisely known. In other words, the integrated changes in the period are well determined but not knowing the rate of change everywhere, the instantaneous sidereal periods are less-well constrained. As a consequence, absolute values for rotational phases are

Table 5. Summary of Results for Wirtanen Model Parameters

Nucleus parameters:			
Pole obliquity			70°
Pole orbital longitude (i.e. principal angle)			240°
Pole R.A.			319°
Pole Declination			-5°
Maximum sidereal rotation period			9.14 hr
Source Regions:			
	Latitude	Longitude	Radius
Primary	-5°	130°	50°
Secondary	-20°	290°	40°

also unknown, and the phase values given for specific images are only appropriate in a relative sense within an observing run. With these caveats, along with the requirement that the source longitudes remain fixed, we were able to establish the absolute source locations. Specifically, the primary source is centered at 130° longitude, while the secondary source is centered at 290° , each with uncertainties of less than 10° , and where the fiducial of 0° longitude is defined as the anti-sunward direction at time of perihelion.

5.6. The Overall Model Solution

Our resulting, overall model solution is summarized as follows, based on our attempts to match the morphological features seen during full rotational cycles during a three-month interval. Basic parameters, including the pole orientation and source centers and sizes, are presented in Table 5. Already noted in Section 5.4 was the large change in both the sub-solar and sub-Earth latitudes during the apparition, shown in the top panel of Figure 7. The 3-D pole orientation of the nucleus, as seen from Earth, also varied drastically with time. To better understand the rotational motion projected on the sky plane, the bottom panel of Figure 7 plots both the projected position angle of the positive (northern) pole, and the angle of the pole to the plane of the sky where $+90^\circ$ corresponds with the pole pointing directly towards Earth.

Representative images, chosen to exhibit distinctive features throughout the apparition, are presented as a series of quadruple frames in Figures 9–12. In each case, we show the CN image, enhanced using azimuthal average (left) and using temporal average (center-left) along with the corresponding model solution (center-right). Additionally, we show a side-on view of the model (far-right) from the right side orthogonal direction to better understand the 3-D characteristics of the jets. Because

of the large width of each jet, a considerable portion of each rotational cycle has overlapping features as seen in projection on the sky. While these are not nearly as constraining as those with clear features, a few are shown for completeness. An advantage of the model is that we can color-code the jets, and we have assigned yellow to the primary jet, whose source is centered at -5° latitude, while we use green for particles originating from the secondary jet centered at -20° . As already noted, in addition to the broad width of each jet simply due to the very large source radius, 50° and 40° respectively, there is significant additional dispersion due both to the daughter excess velocity and a Gaussian spread from the normal direction at each location within the source regions.

Looking first in detail at the panels of Figure 9, note that the features in the top and bottom row of images are readily separated into the primary (yellow) and secondary (green) jets but that the apparent single misshapen spiral in the middle row temporal enhanced image is, in fact, the overlap of the two jets, each dominating in different regions of position angle. Also note the arrows showing the projected direction of the Sun (yellow far-left and magenta far-right) along with the projected rotation axis of the nucleus (cyan right and far-right). While the jet morphology first appears as if one is viewing from nearly pole-on, in fact the pole is nearly in the plane of the sky, and as previously discussed the very broad jets produce this planetary nebula effect. The images enhanced with the azimuthal average clearly are brightest towards the lower-left, consistent with the phase lag of 1–2 hours with activity strongest in the local early afternoon; this characteristic is not included in the model, which is therefore brightest in the solar direction.

As is evident by the projected pole orientation in the side-on model views in Figures 10 and 11, the Earth crosses the equatorial plane only two days before perihelion (see also Figure 7). With the center of the primary jet located at -5° , nearly equal amounts of material are released to the north (left) and south of our view on December 10 (Figure 10, top row) while the secondary jet has a greater amount toward the southern hemisphere. In contrast, only a week before (Figure 10, middle and bottom rows), the clockwise rotation is still visible. We attribute some of the apparent mismatches between the model and the images in the bottom row of Figures 10 and 11 to our model assuming uniform activity across the entire source region while any actual region subtending $\sim 90^\circ$ would naturally have pockets of higher or lower activity. Finally, by January the overall morphology has a clear counter-clockwise rotation (Figure 12), and the

model provides an excellent match throughout the rotational cycle, often with what appears to be a single feature but is actually an overlap of the two jets.

As is evident by simply comparing the two types of enhancements to the CN images, while the majority of the gas throughout the apparition is on the sunward side from the nucleus, as would be expected, a non-negligible amount of material is seen on the other side. While some of this anti-sunward material is simply due to projection effects, the model confirms that material must be continuing to be released from the nucleus even when the Sun is not illuminating the surface, as evidenced by the full spirals associated with the primary source. A first-cut result is that the CN parent is being released during the night at about 10% of the rate as when the Sun is at the local zenith, and this value is included in the model. However, it is unknown whether this is due to a slow thermal lag of basic water ice vaporization or due to ongoing vaporization of CO or CO₂. Additionally, we see clear evidence for short-term thermal lag of about an hour. When closely examining the relative brightness of features as a function of position angle in the azimuthal enhancement, the true peak in release rates comes not when the Sun crosses the meridian, but up to an hour later. Indeed, we also see evidence for a lag at dusk, with more material released following sunset than at a corresponding time prior to sunrise. Since such short lags are not included in the model, we simply note these characteristics here but made no attempt to reproduce them.

As a relatively simple model, having a spherical nucleus with just two circular active regions, the model overall works remarkably well. In fact, there were only two instances when there were notable issues. The first was on December 12 which, as detailed in Paper I, was during the aftermath of a significant outburst, and the “standard” morphology was overwhelmed by material released in the outburst. Once the cause of the discrepancy was identified, we stopped further model analysis. The second took place only a few days later (December 16 and 17) when a persistent feature was evident in the CN images very close to the nucleus at a P.A. of ~ 60 – 90° , and that apparently did not change in appearance with rotation. Examination of the continuum images confirmed that this was a dust feature contaminating the CN filter images. Note that the timing was just days prior to the comet reaching minimum phase angle and just following the Earth’s crossing of Wirtanen’s orbital plane. Thus a tail would have had the greatest projection effect and would appear both shorter and brighter than at other times. It is also possible that larger, very slow moving grains released in the December 12 out-

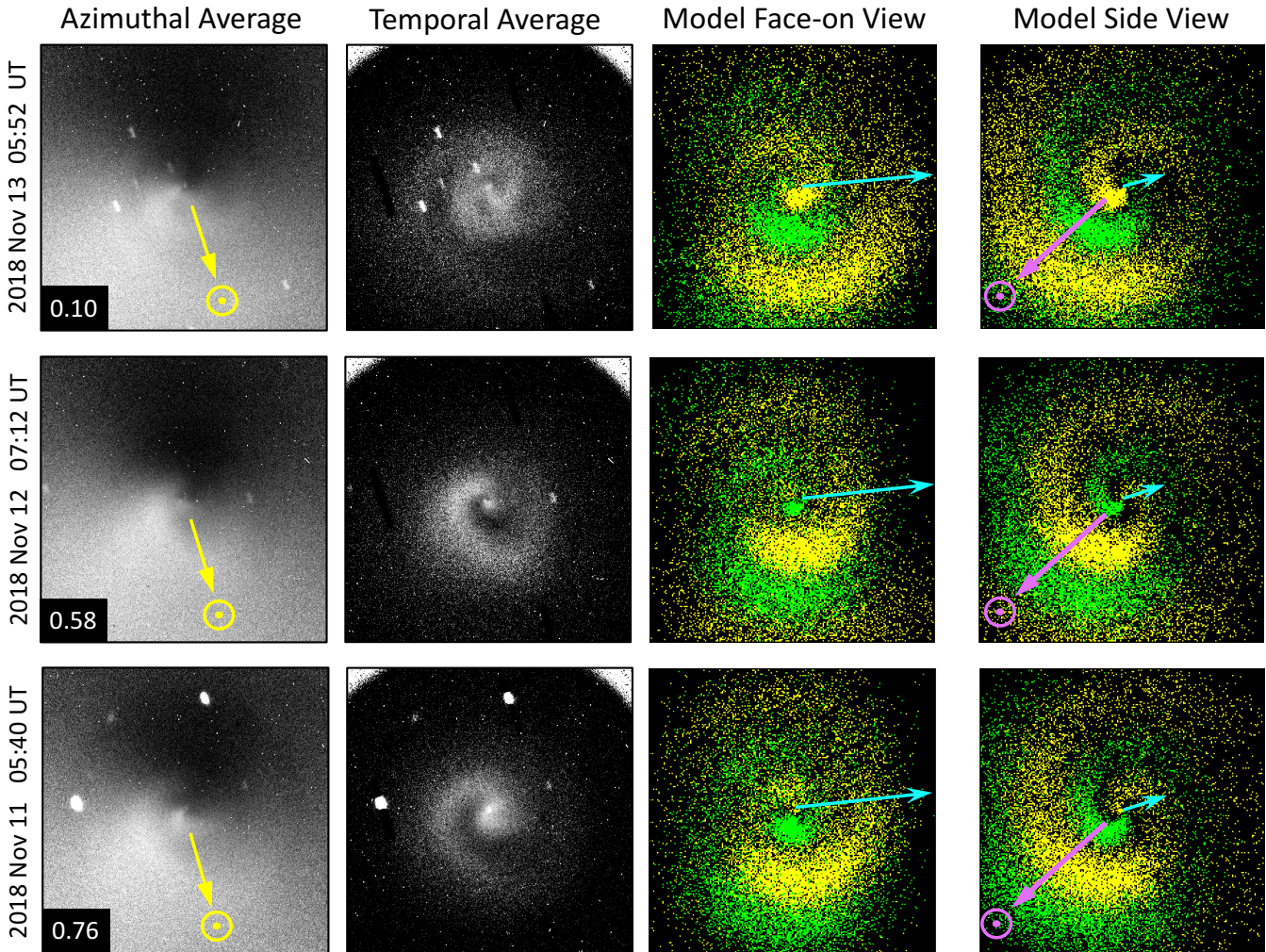


Figure 9. Representative images and corresponding model solutions from 2018 November 11–13. The first two columns contain enhanced CN images (enhancements given above the columns) with north up and east left, while the third column is as seen from Earth and the fourth column is as seen from the perpendicular direction from the right. All images on a row are for the time specified to the left of the first image. The rotational phase is given on the first panel of each row (see text for details). The direction to the Sun is indicated in yellow in the first column (valid for columns 1–3) and in magenta in the fourth column (valid for column 4). The turquoise arrow in the third and fourth panels indicates the projected direction of the north rotation pole (the differing lengths indicate the amount of projection for that view). The yellow and green points in the model images correspond to material emitted from the primary and secondary source regions, respectively, as further described in the text. All images are 60,000 km on a side and are centered on the nucleus.

burst might have finally moved beyond the seeing disk. Whatever the cause, and having failed to reproduce this feature with the existing model (even by attempting to add a third, small source region), we ultimately ignored this stationary inner-coma feature. Finally, note that the second outburst reported in Paper I, that was evident in *R*-band images on January 28, was smaller than the December 12 outburst and not detected in the CN morphology.

Other, ongoing differences between the images and the model we attribute to limitations of the model. We

are certain that Wirtanen’s nucleus is not spherical in shape, and also that local topography will play a role. Source regions won’t simply be circular, and are unlikely to be uniformly active over their entire region. Most surprising is how regular the overall activity is every rotational cycle, perhaps because of the large size of the source regions: as ice is vaporized away in some sub-regions, more ice is exposed in other areas but all within the same broad feature. We also acknowledge that, based on spacecraft imaging of several comets, there are undoubtedly other, smaller active regions dis-

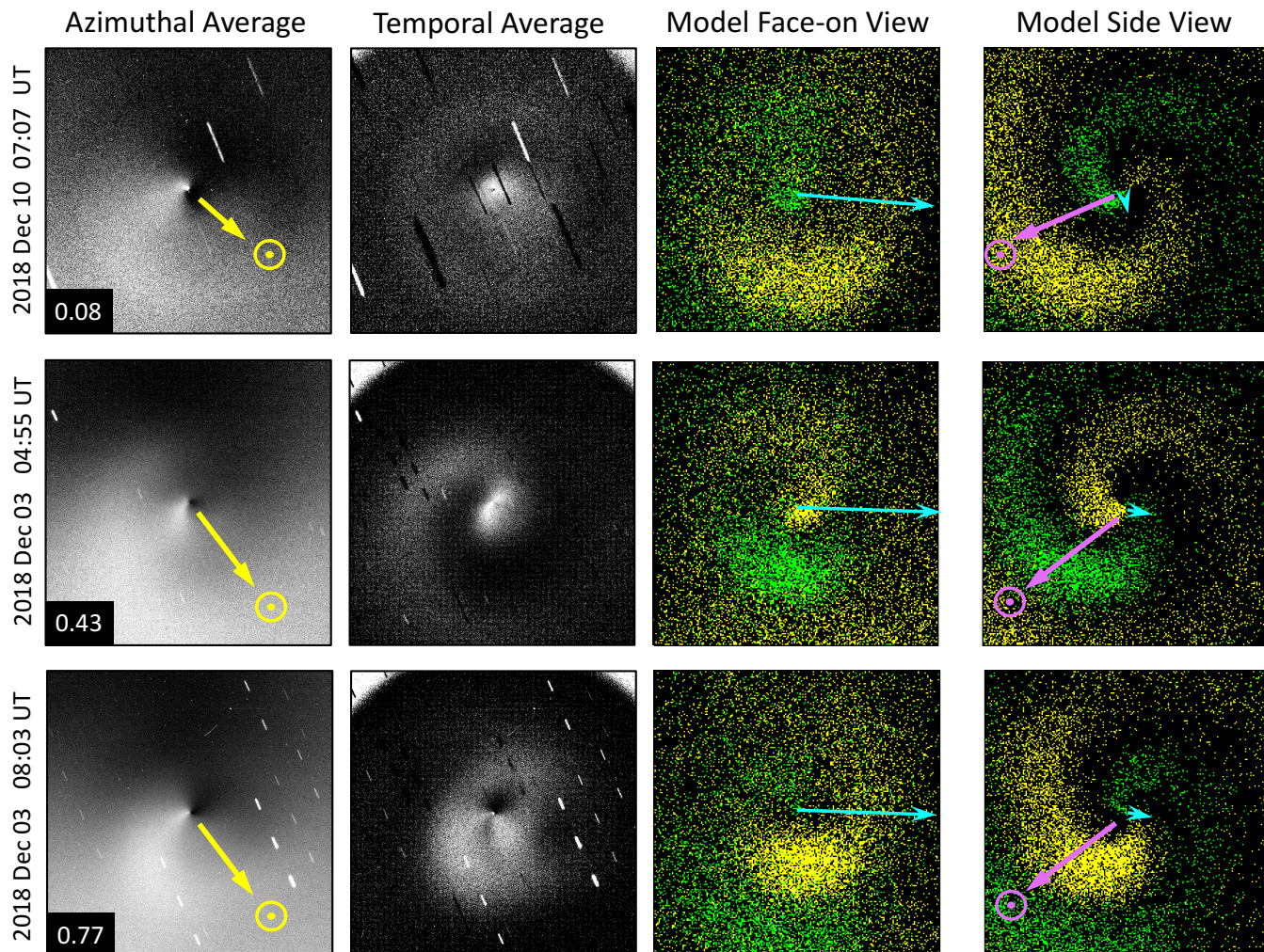


Figure 10. Representative images and corresponding model solutions from 2018 December 3–10. Images as described in Figure 9 except that the images are 30,000 km across.

tributed across the remainder of the nucleus’ surface, but that the majority of the coma material arises from the two large source regions that we have identified here.

Our model assumes simple, i.e., principal axis, rotation. As discussed in Paper I, the CN morphology repeated very well from cycle-to-cycle and night-to-night suggesting this was a valid assumption. We did not see evidence for systematic or repeating deviations in CN morphology compared to our model which might indicate a non-principal axis component to the rotation. Thus, we conclude that our assumption of simple rotation is safe and that any non-principal axis rotation is small or non-existent.

6. DISCUSSION

6.1. Synergistic aspects of imaging, modeling, and photometry

The recent, excellent apparition of Comet 46P/Wirtanen provided an unusual opportunity to obtain both narrowband photometry and imaging over a wide range of distances and viewing geometries. Each method of investigation provided interesting and sometimes unexpected results, but when combined with a successful model of the gas jet morphology, a complete and self-consistent characterization of Wirtanen’s nucleus is revealed.

For instance, measured production rates of the carbon-bearing species (CN, C₂, and C₃) exhibit little to no asymmetry before and after perihelion. Not only is this lack of a pre-/post-perihelion asymmetry atypical of Jupiter family comets (A’Hearn et al. 1995), it would generally imply that the nucleus had a low obliquity and thus minimal seasonal variations. However, the model solution yielded a quite large obliquity (70°), and only

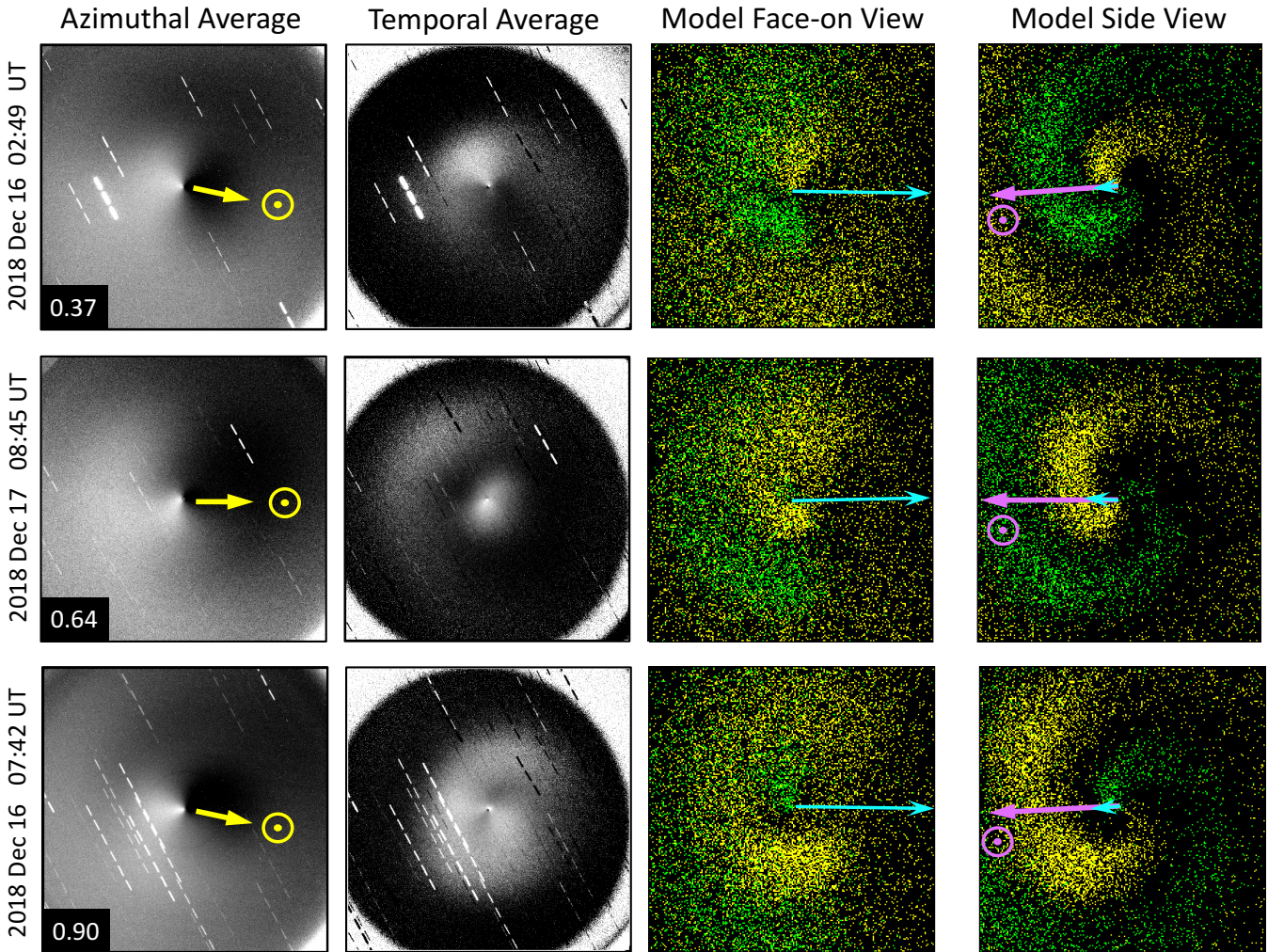


Figure 11. Representative images and corresponding model solutions from 2018 December 16–17. Images as described in Figure 9 except that the images are 30,000 km across.

the fact that the major source regions were located very close to the equator prevented the correspondingly large seasonal effects. Examination of the images obtained near closest approach to Earth revealed another puzzle: the distinct spiral structures observed in early November were replaced by an overall top-to-bottom motion of fairly diffuse features. Only with the modeling did it become clear that the jets were extremely broad and that we (at Earth) took many weeks to traverse across the jets as they swept by the Earth each rotational cycle. This also meant a continually changing overlap pattern of the two jets, adding to the complexity of the observed morphology. Ultimately the spiral pattern returned in January, but with the opposite sense of rotation due to our then viewing the comet from the other hemisphere, having completed our crossing of the equatorial plane.

Other key findings include the discovery of two major source regions, both extending across the equator but at nearly opposite longitudes. This explains the similar but yet distinct appearance of alternating spiral structures seen in the CN gas images early and late in the apparition. The spacing of the alternated jets was nearly the same but one jet had complete spirals while the other one’s were either incomplete or swept by the Earth and were therefore difficult to detect. Ultimately, modeling revealed that the same two features (and thus the same source regions) dominated activity throughout the apparition, but that the smaller and more southerly located source region was proportionally less important late in the apparition when the sub-solar latitude was far to the north. However, since no pre-/post-perihelion production rate asymmetry is evident for the carbon-bearing species, the southern source’s center at -20°

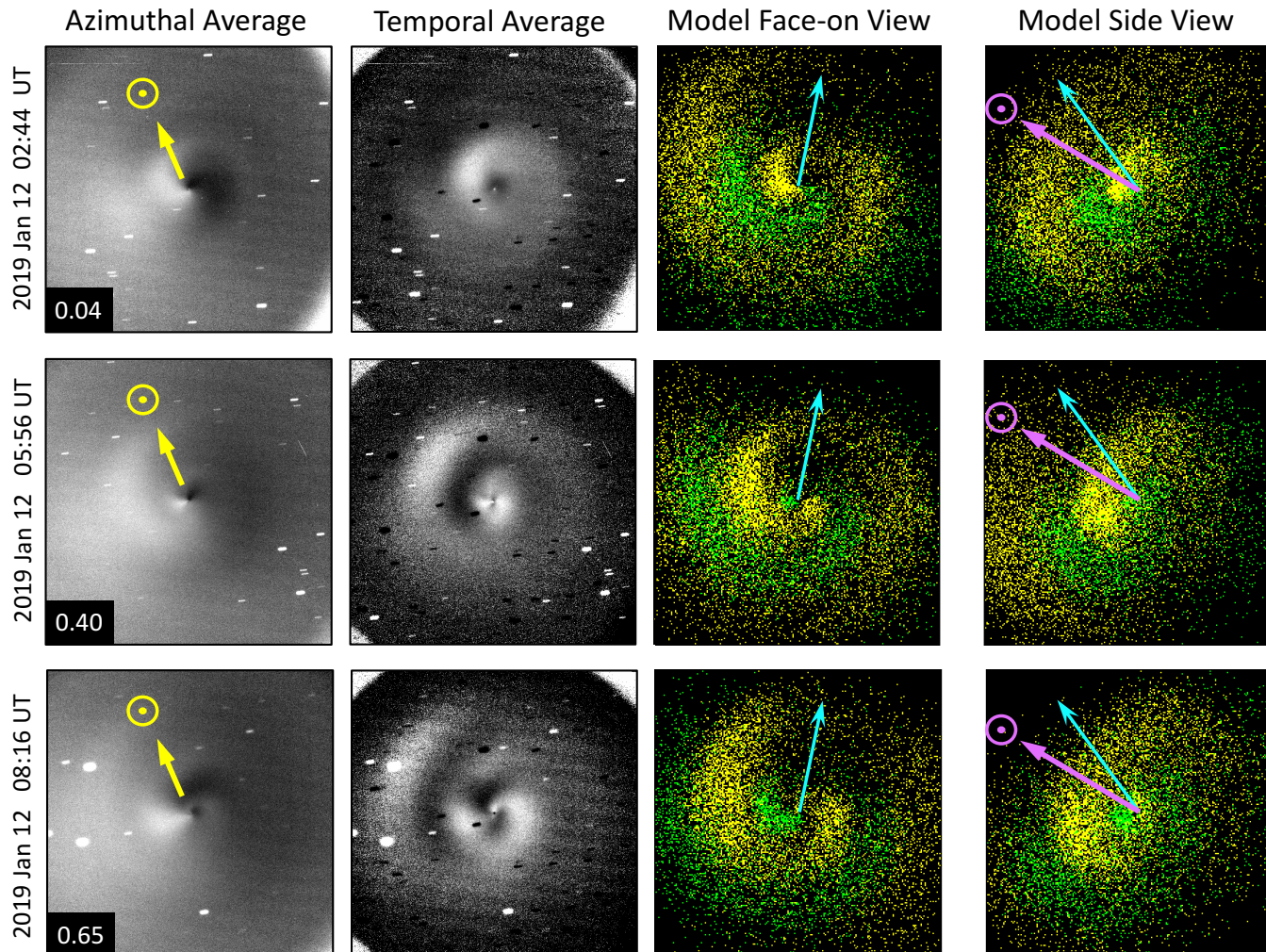


Figure 12. Representative images and corresponding model solutions from 2019 January 12. Images and scale as described in Figure 9.

coupled with the Sun being directly overhead in October compensated for the Sun crossing the equator nearly a month prior to perihelion. The longitudinal separation of the sources (160°) also naturally explains our finding from Paper I that the lightcurve peaks were separated by an effective longitude of $\sim 170^\circ$.

6.2. *Inter-species comparisons*

Unlike the carbon-bearing species, that show clear jet structures in their morphology and no production rate asymmetries about perihelion, the hydrogen-bearing species (OH and NH) are significantly different in both respects. The r_H -dependencies of OH and NH are only slightly steeper than the carbon species prior to perihelion with log-log slopes near -4.3 , but were both significantly steeper (slopes near -5.1) outbound. If one uses water (i.e., OH) as the fiducial, then the simple explana-

tion is that there is a difference in the abundance ratio of the carbon species between the two source regions with the higher abundance of carbon in the primary (equatorial) source region.

Another difference between hydrogen-bearing and carbon-bearing species is that OH and NH show little to no evidence of jet morphology that is clear in CN and the carbon-chain species. Moreover, there is a bulk enhancement in the anti-sunward hemisphere, indicating that a significant portion of OH and NH arise from icy grains. This tailward asymmetry is not, however, equally distributed on either side of the dust tail, but is enhanced towards the peak in brightness of the carbon-bearing jets, i.e., it appears that icy grains are released from the same source regions as create the CN jets, but these grains are then pushed in the anti-solar direction by solar radiation pressure. Because no motion of the

bulk OH morphology is evident during a rotation cycle, nor is jet-like structure seen, we think that the grains must be relatively large and slow moving. Also, having an icy grain source would effectively make OH a granddaughter species, further dispersing the OH. Why these icy grains contain water and ammonia but not the carbon-bearing species remains a mystery, but Wirtanen is only the latest of several comets displaying such behavior, including 103P/Hartley 2 (Knight & Schleicher 2013), C/2013 R1 Lovejoy (Opitom et al. 2015), and 252P/LINEAR (Knight & Schleicher 2016) Unfortunately, we were unable to assess if the proportion of OH and NH arising from icy grains was related to the steeper r_H -dependencies measured after perihelion, or if the proportions of icy grains arising from the two source regions are similar. The lack of rotational variation in OH and NH morphology and the limited number of narrowband images prevented us from assessing if the relative abundances in the two source regions varied with time. It is unlikely that the flatter pre-perihelion OH and NH r_H -dependencies was due to the presence of a large population of icy grains released significantly before perihelion since, at these heliocentric distances, the lifetime of such grains should be relatively short (hours to days; Beer et al. 2006) compared to the temporal span of our observations.

The primary attributes of the dust coma are also interesting. A clear dust tail is seen but the background dust coma is brighter towards the peak in CN brightness, similar to that for OH. Dust jets are not detected, but we attribute this lack of discrete features as being due to much lower outflow velocities coupled with a large dispersion in particle sizes and the associated large dispersion in velocities. This combination would effectively wipe out any features. Somewhat of a surprise is that the dust abundance, as measured by $Af\rho$ and following adjustments for phase angle and aperture size, has an r_H -dependence the same on either side of perihelion, i.e., matching the carbon-bearing species. This raises the intriguing possibility that H_2O may not be the primary driver of Wirtanen’s activity, or at least that another volatile parent species contributes non-negligibly. However, Wirtanen was found to be poor in CO (Biver et al. 2019a; Saki et al. 2020), while derived atomic production rates in the far UV suggest that CO_2 and O_2 were “not abundant” in comparison to H_2O (Noonan et al. 2021). Thus, there is no obvious volatile species that might explain the behavior.

6.3. Long-term Secular Decrease in Production Rates

Comet Wirtanen exhibited a strong decrease in both gas and dust production rates since the 1990s. In fact,

our data show a monotonic decrease from 1991 to 1997, then to 2008 and now to the 2018 apparition. Due to the comet’s greatly differing distances from Earth, and the corresponding projected aperture sizes, we looked for aperture effects associated with our Haser model parameters for each gas species and eliminated this as a cause. There was, as with most comets, a significant aperture effect for $Af\rho$, for which we measured and corrected. Also adjusting for phase angle effects, $A(0^\circ)f\rho$ showed a very similar amount of secular decrease as the gas species: just over a factor of two. Our results are very similar to that reported by Combi et al. (2020) from 1997 to 2018, who also claimed a factor of two near perihelion and an even larger decrease at larger distances. Combi et al. also found that Wirtanen had substantially higher values for most of 2002 than in 1997, but large variations in only a few days on multiple occasions strongly indicate that most of their 2002 observations were dominated by outburst activity. Thus, the ensemble evidence suggests that the underlying activity level (sans outbursts) indeed has been continuing to decrease for the past 20–30 years.

This rate of drop in production rates, while unusual, is not unprecedented. Of the 18 comets in our photometry database for which we have multi-apparition data suitable for investigating secular changes, only a handful exhibit clear changes not attributable to a change in perihelion distance. In particular, Comet 9P/Tempel 1 had decreases by factors of 1.5 to 2.4 depending upon species between 1983 and 2005 (Schleicher 2007), while the most extreme case is 103P/Hartley 2, where all species decreased by a factor of ~ 3 from 1991 to 2010/11 (Knight & Schleicher 2013). One common attribute of Hartley 2 and Wirtanen is that each had fairly recently undergone a major orbital change from significantly larger perihelia due to close passages with Jupiter. Hartley 2 suffered a large perturbation in 1971, with a decrease in perihelion from 1.67 AU to 0.90 AU and had crept back to 1.06 AU by 2010. Wirtanen’s perihelion decreased from 1.61 AU to 1.26 AU in 1972, followed by another drop to 1.08 AU in 1984 (it is now at 1.05 AU). The other notable attribute is that both objects were classified as “hypervolatile” based on their water production rates being higher than could be understood by vaporization of their small nucleus surface areas. Indeed, both exhibit strong evidence of icy grains, explaining the hyperactivity. What is unclear is how these two characteristics relate to one another. Are icy grains associated with the decrease in perihelia and the resulting higher surface temperatures, i.e., are icy grains preferentially released in these circumstances? Also, are the decreasing total production rates associated with a decrease in

the amount of icy grains? The latter possibility appears to *not* be the case, as the icy grains apparently do not include carbon-bearing species and yet all species show the same secular decrease.

6.4. Fractional Active Areas of the Jet Source Regions

Based on our modeling of the two jets throughout the 2018/19 apparition, we concluded that the primary source region had a radius of $\sim 50^\circ$ while the secondary source was also quite large, having a radius of $\sim 40^\circ$ (18% and 12% of the total surface area, respectively). This is near the high-end for the sizes of jets derived from coma models, but it is not anomalous. Comets C/1995 O1 Hale-Bopp and 67P/Churyumov-Gerasimenko exhibited jets of radii $15\text{--}30^\circ$ (Vasundhara & Chakraborty 1999; Schleicher et al. 2004; Schleicher 2006), and C/2007 N3 Lulin had jets of 10° and 20° (Bair et al. 2018), but the most comparable comet previously modeled was C/1996 B2 Hyakutake (Schleicher & Woodney 2003), which had a primary source of $\sim 56^\circ$ radius (and a smaller secondary source of $\sim 16^\circ$).

In 2018, Wirtanen’s measured active fraction was 55%. This suggests that the 30% of the surface covered by the two jet sources represents a significant portion of the comet’s activity if we assume that the source of the CN also reflects the source of water. Indeed, given that independent evidence suggests that part of the water is emitted from grains in the coma, it is likely that the two jet sources represent the majority of the comet’s activity. The extent of these active areas, distributed over a non-spherical nucleus increases the likelihood that ejected material will produce reactionary forces that do not pass through the nucleus’ center of mass, resulting in torques that can alter the comet’s rotation. This is discussed further in the next subsection.

Regardless of whether we assume that the active fraction is 55% based on water production rate or 30% based on CN jet modeling, it is evident that Wirtanen is still a “young” comet having ample volatile ices near the surface. Assuming that active fraction decreases as a comet spends more time in the inner solar system due to loss of accessible volatiles and/or mantling over of the surface, a larger active fraction should be indicative of a younger comet. Of 38 Jupiter family comets having measured nucleus sizes in our photometric database (Schleicher & Bair 2016), 27 have smaller active fractions than 30% (our more conservative number), and two-thirds of these are smaller than 10%. Our database also reveals that active fractions of Jupiter family comets generally decrease with decreasing perihelion distance. Wirtanen’s active fraction is high compared to the subset with comparable perihelion distances, further evidence that it has not

spent as much time in the inner solar system. We note, however, that this assessment of “youth” greatly simplifies a host of potentially competing factors including compositional differences and unknown dynamical histories, and competing interpretations exist (e.g., Belton 2010; Vincent et al. 2017).

6.5. The Rotation Spin-down and Spin-up

A major result from our studies was the change documented in the rotation period of Wirtanen, and the nature of that change in light of the modeling results. Before perihelion, the rotation period increased by $\sim 4\%$ (Farnham et al. 2021), only to decrease again after perihelion to a value similar to what it was at the start of the apparition, indicating that the net torques on the nucleus are significant, yet they are highly seasonal and largely cancel out when integrated over the perihelion timeframe. This is likely due to the sizes and relative locations of the two active areas, which produce net torques that change as the sub-solar latitude shifts north.

One scenario that would explain the observed changes involves a prolate spheroid nucleus rotating about its small axis (consistent with the radar estimate of the nucleus being 1400×1100 m; E. Howell, priv. comm.), with the two jets placed at angles $\sim 10^\circ$ from each end, where the moment arms are long. Because the jets are effectively 160° apart in longitude, they are offset on the same side of the body, producing torques in opposite directions. When the Sun is in the southern hemisphere, the smaller jet receives more direct insolation and thus dominates the torques during the pre-perihelion timeframe, slowing the nucleus’ spin. As the Sun moves north, the southern jet weakens and the equatorial jet, producing torques in the opposite direction, becomes dominant, spinning the comet up again. Although this scenario qualitatively explains the observations, it is a simplistic depiction and is by no means unique.

The only other comet known to exhibit a rotational change in which the period reverses direction in the middle of an apparition is comet 67P/Churyumov-Gerasimenko, which spun down slightly during its approach to the Sun before spinning up more dramatically around perihelion (Keller et al. 2015; Kramer & Läuter 2019). However, there are significant differences between Wirtanen and 67P, in that 67P did not exhibit significant isolated jet activity (the rotation rates were detected from *Rosetta* observations of the nucleus, as opposed to lightcurves or coma morphology) nor did 67P show the degree of volatile release from icy grains exhibited by 103P (A’Hearn et al. 2011; Protopapa et al. 2014) or (based on our study) Wirtanen (e.g., Gasc et al.

2017; Biver et al. 2019b; Protopapa et al. 2020). Thus, the torques on the nucleus arose from the integrated activity across the non-spherical nucleus, and the extreme seasonal differences between the northern and southern hemispheres (active during the approach and perihelion timeframes, respectively) resulted in the rotation reversal.

It is difficult to assess how common this phenomenon might be since few comets are observed well enough over a sufficient baseline. Rotation periods are easiest to determine for comets with weakly active or inactive nuclei, where photometry can measure the light reflected from the rotating nucleus directly. This is possible either when comets are far from the Sun and their activity has decreased or at any time for intrinsically low activity comets. In both cases, the weak activity cannot provide the torquing needed to change the rotation period except under highly favorable scenarios and, in the distant observation case, the geometry change is likely to be very slow. Thus, morphological studies or inner coma lightcurves are the most promising ways to detect changing rotation periods over short timescales. However, they require bright comets with reasonably small geocentric distances, favorable morphology, and/or short rotation periods. Over the last decade, only two other comets have yielded similar coverage of the rotation period as Wirtanen: 103P/Hartley 2 (e.g., Knight & Schleicher 2011; Samarasinha et al. 2011; Belton et al. 2013; Knight et al. 2015) and 41P/Tuttle-Giacobini-Kresák (Bodewits et al. 2018; Schleicher et al. 2019). In both cases, much larger rotation period changes were detected than for Wirtanen, but the change was always in the same direction. Neither comet has yet been modeled with a fully self-consistent solution that reproduces the coma morphology, but their monotonic changes in period suggest that neither has a scenario similar to Wirtanen.

Without several epochs of extensive observations in a single apparition, it is impossible to detect a small and reversing change in the rotation such as we measured for Wirtanen. The increase/decrease in the rotation period raises an interesting question: How much did the rotation state change and how does this factor into comparative studies with other comets? If we consider the start and end points for the rotation period found in Paper I (e.g., the change per orbit), then Wirtanen would be considered to exhibit little rotational variability. On the other hand, we observe an increase and then a decrease totaling ~ 21 min ($\sim 4\%$ of the rotation period), within a few months of perihelion, indicating that there are significant variations occurring over time. Other comets could exhibit similar tendencies, with sea-

sonal effects producing opposite trends that cancel out over the course of the orbit. Thus, objects known to have monotonic changes from apparition-to-apparition or even no change might be experiencing similar behavior to Wirtanen. In fact, this is exactly the case for 67P which, in the absence of *Rosetta* data, would be judged to have a monotonic period change. Without comprehensive models of pole orientation and jet location and extent, it is difficult to determine the cause of these changes.

Another result of our modeling is how Wirtanen challenges predictions of changes in rotation period that are based on behavior being globally similar between comets. As just discussed, Wirtanen’s change in rotation state is quite different from that of Hartley 2, a superficially similar object (see discussion in Paper I). The model of Samarasinha & Mueller (2013) and Mueller & Samarasinha (2018) uses overall activity and nucleus size to predict changes in rotation period. Their methodology predicts a period change of 18 min for Wirtanen. We measured a +9 min then a -12 min change, so either it is a very good prediction (for a total change of 21 min), off by $\sim 50\%$ (for either the spin-down or spin-up considered in isolation), or substantially off (for the ~ 2 min net change over the apparition). Rafikov (2018) predicted changes in the rotation periods of comets based on measured non-gravitational accelerations. Given Wirtanen’s relatively large rate of period change over small segments of its orbit, it would be viewed as very prone to spin evolution if only observed during these portions, while its spin evolution would be viewed as relatively modest when considered on an orbit-by-orbit basis. An investigation of Wirtanen’s non-gravitational forces during the subsets of time in which we saw the largest period changes would be an interesting test of the Rafikov model, though it is beyond the scope of this paper.

7. CONCLUSIONS

We successfully conducted a multi-faceted observing campaign of Comet 46P/Wirtanen during its historically close approach to Earth in 2018/19. These data, combined with photometric observations from three prior apparitions, and detailed modeling of the recent imaging, permitted us to obtain a much more complete understanding of this “hyperactive” comet than previously had been obtained despite it having been the original target of ESA’s *Rosetta* mission.

Paper I (Farnham et al. 2021) presented results from our extensive CN imaging, finding a continuously changing rotation period that first increased then decreased. The interconnected studies presented here provide a

means to explain and interpret the findings in Paper I. These include:

- Gas production rates are symmetric about perihelion for carbon-bearing species (CN, C₃, and C₂), but fall off more steeply post-perihelion for OH and NH. Despite the different trends, the composition remained “typical” throughout our observations.
- There is an ongoing secular decrease in gas activity and dust production over four apparitions: 1991, 1997, 2008, 2018 (we did not obtain data in 2002 or 2013).
- The carbon-bearing species exhibit similar coma morphology that varies with rotation. The coma morphology of OH, NH, and dust did not change appreciably with rotation. We attribute the appearance of OH and NH to their having a significant source from icy grains in the coma, while the lack of rotational signal of these and the dust is due to the lower velocities and larger velocity dispersion among grains as compared to gas.
- Our preferred model replicates the cycle-to-cycle variation of the two CN jets identified in Paper I as well as the evolution over the apparition of their senses of rotation and relative brightnesses. The model has two large, mid-latitude jets and a pole oriented at R.A. = 319°, Declination = −5°, based on an obliquity of 70° and a principal angle of 240°.
- The primary jet has a radius of 50° and is centered at a latitude and longitude of (−5°, 130°), while the secondary jet is 40° in radius and is at (−20°, 290°). The seasonal variation in production rates can, therefore, be explained if there is compositional heterogeneity between the source regions, with the northern region having a higher abundance of carbon.
- The fractional active area in 2018/19 is ~55%. Our modeling suggests the source regions cover ~30% of the surface, implying that they represent the plurality of surface activity. The imaging suggests that much of the excess OH signal (above 30%) may come from icy grains in the coma. Regardless of which measure is used to assess active area, Wirtanen is at the high end of our photometry database and appears to be a “young” surface.
- Our model demonstrates that the changing rotation period discovered in Paper I represents a

change in the sidereal period and is not due to changing viewing geometry alone. It also provides a natural explanation for the alternately increasing then decreasing sidereal rotation period as being due to the evolving dominances of the two source regions as their seasons change during the apparition. Such behavior is difficult to diagnose without extensive observations and, if common, likely skews our understanding of the stability of comet rotation periods.

Our findings, in concert with the diverse results obtained by the community over the same time period are a reminder that, for highly favorable apparitions such as Wirtanen, major new insights into and significant constraints on physical properties of comets can be obtained at a fraction of the cost of a spacecraft. Nonetheless, space missions are unrivaled in providing specific details which cannot be obtained remotely. Due to its orbital characteristics, Wirtanen has long been a prime mission target and continues to be proposed for a future spacecraft mission; our many findings should prove very useful in planning such missions.

We gratefully acknowledge Lori Feaga, Dennis Bodewits, Josie Schindler, Brian Skiff, Uwe Konopka, Carrie Holt, and Larry Wasserman for assisting with some of the observations, and Allison Bair for assisting with the photometric analyses and construction of tables. We thank the anonymous referees for prompt and helpful reviews. This work was supported by NASA Solar System Observations Program grants 80NSSC18K0856 and 80NSSC18K1007, Hubble Space Telescope grant HST-GO-15372, and NSF award AST1852589. These results made use of the Lowell Discovery Telescope (LDT) at Lowell Observatory. Lowell is a private, non-profit institution dedicated to astrophysical research and public appreciation of astronomy and operates the LDT in partnership with Boston University, the University of Maryland, the University of Toledo, Northern Arizona University and Yale University. The Large Monolithic Imager was built by Lowell Observatory using funds provided by the National Science Foundation (AST-1005313).

Facilities: Lowell Discovery Telescope, Lowell Observatory 42 inch (1.1 m) Hall Telescope, Lowell Observatory 31 inch (0.8 m) telescope.

Software: IDL

REFERENCES

- A'Hearn, M. F. 1991, *Photometry and Polarimetry Network*, ed. Sekanina, Z. & Fry, L., 193
- A'Hearn, M. F., Millis, R. L., Schleicher, D. G., Osip, D. J., & Birch, P. V. 1995, *Icarus*, 118, 223, doi: [10.1006/icar.1995.1190](https://doi.org/10.1006/icar.1995.1190)
- A'Hearn, M. F., Millis, R. L., & Thompson, D. T. 1983, *Icarus*, 55, 250, doi: [10.1016/0019-1035\(83\)90080-5](https://doi.org/10.1016/0019-1035(83)90080-5)
- A'Hearn, M. F., Schleicher, D. G., Millis, R. L., Feldman, P. D., & Thompson, D. T. 1984, *AJ*, 89, 579, doi: [10.1086/113552](https://doi.org/10.1086/113552)
- A'Hearn, M. F., Belton, M. J. S., Delamere, W. A., et al. 2011, *Science*, 332, 1396, doi: [10.1126/science.1204054](https://doi.org/10.1126/science.1204054)
- Bair, A. N., Schleicher, D. G., & Knight, M. M. 2018, *AJ*, 156, 159, doi: [10.3847/1538-3881/aad549](https://doi.org/10.3847/1538-3881/aad549)
- Baum, W. A., Kreidl, T. J., & Schleicher, D. G. 1992, *AJ*, 104, 1216, doi: [10.1086/116310](https://doi.org/10.1086/116310)
- Beer, E. H., Podolak, M., & Prialnik, D. 2006, *Icarus*, 180, 473, doi: [10.1016/j.icarus.2005.10.018](https://doi.org/10.1016/j.icarus.2005.10.018)
- Belton, M. J. S. 2010, *Icarus*, 210, 881, doi: [10.1016/j.icarus.2010.07.007](https://doi.org/10.1016/j.icarus.2010.07.007)
- Belton, M. J. S., Thomas, P., Li, J.-Y., et al. 2013, *Icarus*, 222, 595, doi: [10.1016/j.icarus.2012.06.037](https://doi.org/10.1016/j.icarus.2012.06.037)
- Biver, N., Bockelée-Morvan, D., Crovisier, J., et al. 2019a, in *EPSC-DPS Joint Meeting 2019*, Vol. 2019, EPSC-DPS2019-116
- Biver, N., Bockelée-Morvan, D., Hofstadter, M., et al. 2019b, *A&A*, 630, A19, doi: [10.1051/0004-6361/201834960](https://doi.org/10.1051/0004-6361/201834960)
- Bodewits, D., Farnham, T. L., Kelley, M. S. P., & Knight, M. M. 2018, *Nature*, 553, 186, doi: [10.1038/nature25150](https://doi.org/10.1038/nature25150)
- Cochran, A. L., & Schleicher, D. G. 1993, *Icarus*, 105, 235, doi: [10.1006/icar.1993.1121](https://doi.org/10.1006/icar.1993.1121)
- Combi, M. R., Harris, W. M., & Smyth, W. H. 2004, *Gas dynamics and kinetics in the cometary coma: theory and observations*, ed. Festou, M. C., Keller, H. U., & Weaver, H. A. (Univ. of Arizona Press/Lunar Planet. Inst., Tucson, AZ/Houston, TX), 523
- Combi, M. R., Mäkinen, T., Bertaux, J. L., et al. 2020, *The Planetary Science Journal*, 1, 72, doi: [10.3847/PSJ/abb026](https://doi.org/10.3847/PSJ/abb026)
- Cowan, J. J., & A'Hearn, M. F. 1979, *Moon and Planets*, 21, 155, doi: [10.1007/BF00897085](https://doi.org/10.1007/BF00897085)
- Farnham, T. L., & Cochran, A. L. 2002, *Icarus*, 160, 398, doi: [10.1006/icar.2002.6969](https://doi.org/10.1006/icar.2002.6969)
- Farnham, T. L., Kelley, M. S. P., Knight, M. M., & Feaga, L. M. 2019, *ApJL*, 886, L24, doi: [10.3847/2041-8213/ab564d](https://doi.org/10.3847/2041-8213/ab564d)
- Farnham, T. L., Knight, M. M., Schleicher, D. G., et al. 2021, *The Planetary Science Journal*, 2, 7, doi: [10.3847/PSJ/abd091](https://doi.org/10.3847/PSJ/abd091)
- Farnham, T. L., Samarasinha, N. H., Mueller, B. E. A., & Knight, M. M. 2007, *AJ*, 133, 2001, doi: [10.1086/513186](https://doi.org/10.1086/513186)
- Farnham, T. L., & Schleicher, D. G. 1998, *A&A*, 335, L50
- . 2005, *Icarus*, 173, 533, doi: [10.1016/j.icarus.2004.08.021](https://doi.org/10.1016/j.icarus.2004.08.021)
- Farnham, T. L., Schleicher, D. G., & A'Hearn, M. F. 2000, *Icarus*, 147, 180, doi: [10.1006/icar.2000.6420](https://doi.org/10.1006/icar.2000.6420)
- Feaga, L. M., Sunshine, J. M., Knight, M. M., et al. 2018, *Minor Planet Electronic Circulars*, 2018-N81
- Fink, U., & Combi, M. R. 2004, *Planet. Space Sci.*, 52, 573, doi: [10.1016/j.pss.2003.12.002](https://doi.org/10.1016/j.pss.2003.12.002)
- Gasc, S., Altwegg, K., Balsiger, H., et al. 2017, *MNRAS*, 469, S108, doi: [10.1093/mnras/stx1412](https://doi.org/10.1093/mnras/stx1412)
- Helbert, J., Rauer, H., Boice, D. C., & Huebner, W. F. 2005, *A&A*, 442, 1107, doi: [10.1051/0004-6361:20041571](https://doi.org/10.1051/0004-6361:20041571)
- Jeffers, H. M. 1948, *Lick Observatory Bulletin*, 520, 189, doi: [10.5479/ADS/bib/1948LicOB.19.189J](https://doi.org/10.5479/ADS/bib/1948LicOB.19.189J)
- Keller, H. U., Mottola, S., Skorov, Y., & Jorda, L. 2015, *A&A*, 579, L5, doi: [10.1051/0004-6361/201526421](https://doi.org/10.1051/0004-6361/201526421)
- Kelley, M. S. P., Bodewits, D., Ye, Q., et al. 2019, *Research Notes of the American Astronomical Society*, 3, 126, doi: [10.3847/2515-5172/ab3fb4](https://doi.org/10.3847/2515-5172/ab3fb4)
- Kelley, M. S. P., Farnham, T. L., Li, J.-Y., et al. 2020, *Planetary Science Journal*, This volume, Submitted
- Knight, M. M., Mueller, B. E. A., Samarasinha, N. H., & Schleicher, D. G. 2015, *AJ*, 150, 22, doi: [10.1088/0004-6256/150/1/22](https://doi.org/10.1088/0004-6256/150/1/22)
- Knight, M. M., & Schleicher, D. G. 2011, *AJ*, 141, 183, doi: [10.1088/0004-6256/141/6/183](https://doi.org/10.1088/0004-6256/141/6/183)
- . 2013, *Icarus*, 222, 691, doi: [10.1016/j.icarus.2012.06.004](https://doi.org/10.1016/j.icarus.2012.06.004)
- Knight, M. M., & Schleicher, D. G. 2016, in *AAS/Division for Planetary Sciences Meeting Abstracts*, Vol. 48, AAS/Division for Planetary Sciences Meeting Abstracts #48, 217.02
- Knight, M. M., Snodgrass, C., Vincent, J.-B., et al. 2017, *MNRAS*, 469, S661, doi: [10.1093/mnras/stx2472](https://doi.org/10.1093/mnras/stx2472)
- Kramer, T., & Läuter, M. 2019, *A&A*, 630, A4, doi: [10.1051/0004-6361/201935229](https://doi.org/10.1051/0004-6361/201935229)
- Kronk, G. W. 2009, *Cometography: A Catalog of Comets. Volume 4, 1933-1959* (Cambridge, UK: Cambridge University Press)
- Kronk, G. W., & Meyer, M. 2010, *Cometography: A Catalog of Comets. Volume 5, 1960-1982* (Cambridge, UK: Cambridge University Press)
- Kronk, G. W., Meyer, M., & Seargent, D. A. J. 2017, *Cometography: A Catalog of Comets, Volume 6, 1983-1993*, Vol. 6

- Lamy, P. L., Toth, I., Jorda, L., Weaver, H. A., & A'Hearn, M. 1998, *A&A*, 335, L25
- Larson, S. M., Sekanina, Z., & Rahe, J. 1991, *Near-Nucleus Studies Network*, ed. Z. Sekanina & L. Fry, 173
- Lis, D. C., Bockelée-Morvan, D., Güsten, R., et al. 2019, *A&A*, 625, L5, doi: [10.1051/0004-6361/201935554](https://doi.org/10.1051/0004-6361/201935554)
- Mueller, B. E. A., & Samarasinha, N. H. 2018, *AJ*, 156, 107, doi: [10.3847/1538-3881/aad0a1](https://doi.org/10.3847/1538-3881/aad0a1)
- Noonan, J. W., Harris, W. M., Bromley, S., et al. 2021, *The Planetary Science Journal*, 2, 8, doi: [10.3847/PSJ/abd038](https://doi.org/10.3847/PSJ/abd038)
- Opatom, C., Jehin, E., Manfroid, J., et al. 2015, *A&A*, 584, A121, doi: [10.1051/0004-6361/201526427](https://doi.org/10.1051/0004-6361/201526427)
- Osborn, W. H., A'Hearn, M. F., Carsenty, U., et al. 1990, *Icarus*, 88, 228, doi: [10.1016/0019-1035\(90\)90187-E](https://doi.org/10.1016/0019-1035(90)90187-E)
- Protopapa, S., Kelley, M. S. P., Woodward, C. E., & Yang, B. 2020, *PSJ*, submitted
- Protopapa, S., Sunshine, J. M., Feaga, L. M., et al. 2014, *Icarus*, 238, 191, doi: [10.1016/j.icarus.2014.04.008](https://doi.org/10.1016/j.icarus.2014.04.008)
- Rafikov, R. R. 2018, arXiv e-prints, arXiv:1809.05133. <https://arxiv.org/abs/1809.05133>
- Saki, M., Gibb, E., Bonev, B., et al. 2020, in *AAS/Division for Planetary Sciences Meeting Abstracts*, Vol. 52, *AAS/Division for Planetary Sciences Meeting Abstracts*, 212.04
- Samarasinha, N. H. 2000, *ApJL*, 529, L107, doi: [10.1086/312469](https://doi.org/10.1086/312469)
- Samarasinha, N. H., & Larson, S. M. 2014, *Icarus*, 239, 168, doi: [10.1016/j.icarus.2014.05.028](https://doi.org/10.1016/j.icarus.2014.05.028)
- Samarasinha, N. H., & Mueller, B. E. A. 2013, *ApJL*, 775, 5, doi: [10.1088/2041-8205/775/1/L10](https://doi.org/10.1088/2041-8205/775/1/L10)
- Samarasinha, N. H., Mueller, B. E. A., A'Hearn, M. F., Farnham, T. L., & Gersch, A. 2011, *ApJL*, 734, L3, doi: [10.1088/2041-8205/734/1/L3](https://doi.org/10.1088/2041-8205/734/1/L3)
- Schleicher, D. G. 2006, *Icarus*, 181, 442, doi: [10.1016/j.icarus.2005.11.014](https://doi.org/10.1016/j.icarus.2005.11.014)
- . 2007, *Icarus*, 190, 406, doi: [10.1016/j.icarus.2007.04.013](https://doi.org/10.1016/j.icarus.2007.04.013)
- Schleicher, D. G., & Bair, A. N. 2011, *AJ*, 141, 177, doi: [10.1088/0004-6256/141/6/177](https://doi.org/10.1088/0004-6256/141/6/177)
- Schleicher, D. G., & Bair, A. N. 2016, in *AAS/Division for Planetary Sciences Meeting Abstracts*, Vol. 48, *AAS/Division for Planetary Sciences Meeting Abstracts #48*, 308.04
- Schleicher, D. G., & Farnham, T. L. 2004, in *Comets II*, ed. Festou, M. C., Keller, H. U., & Weaver, H. A. (University of Arizona Press, Tucson), 449–469
- Schleicher, D. G., Farnham, T. L., & Hawley, W. 2004, in *AAS/Division for Planetary Sciences Meeting Abstracts*, Vol. 36, *AAS/Division for Planetary Sciences Meeting Abstracts #36*, 25.09
- Schleicher, D. G., Knight, M. M., Eisner, N. L., & Thirouin, A. 2019, *AJ*, 157, 108, doi: [10.3847/1538-3881/aafbab](https://doi.org/10.3847/1538-3881/aafbab)
- Schleicher, D. G., Millis, R. L., & Birch, P. V. 1998, *Icarus*, 132, 397, doi: [10.1006/icar.1997.5902](https://doi.org/10.1006/icar.1997.5902)
- Schleicher, D. G., & Woodney, L. M. 2003, *Icarus*, 162, 190, doi: [10.1016/S0019-1035\(02\)00054-4](https://doi.org/10.1016/S0019-1035(02)00054-4)
- Shou, Y., Combi, M., Toth, G., et al. 2016, *ApJ*, 833, 160, doi: [10.3847/1538-4357/833/2/160](https://doi.org/10.3847/1538-4357/833/2/160)
- Ulamec, S., Espinasse, S., Feuerbacher, B., et al. 2006, *Acta Astronautica*, 58, 435, doi: [10.1016/j.actaastro.2005.12.009](https://doi.org/10.1016/j.actaastro.2005.12.009)
- Vasundhara, R., & Chakraborty, P. 1999, *Icarus*, 140, 221, doi: [10.1006/icar.1999.6105](https://doi.org/10.1006/icar.1999.6105)
- Vincent, J. B., Hviid, S. F., Mottola, S., et al. 2017, *MNRAS*, 469, S329, doi: [10.1093/mnras/stx1691](https://doi.org/10.1093/mnras/stx1691)
- Wang, Z., Zhang, S.-B., Tseng, W.-L., et al. 2020, *AJ*, 159, 240, doi: [10.3847/1538-3881/ab8734](https://doi.org/10.3847/1538-3881/ab8734)